Fabrication of a Superconducting Transmission Line in a Planar Design on a Spin-Doped Crystalline Membrane

THESIS

submitted in partial fulfillment of the
requirements for the degree of

MASTER OF SCIENCE
in
CONDENSED MATTER PHYSICS

Author :	Georg Werner Mair
Supervisor :	Prof. Dr. Rudolf Gross
Advisor :	Dr. Nadezhda Kukharchyk

Garching, April 12, 2023

Fabrication of a Superconducting Transmission Line in a Planar Design on a Spin-Doped Crystalline Membrane

Georg Werner Mair

Walther-Meißner-Institut der Bayerischen Akademie der Wissenschaften
Physik-Department, TUM School of Natural Sciences, Technische Universität München

Garching, Germany

April 12, 2023

Contents

1	**Introduction**	**1**
2	**Theory**	**5**
2.1	Planar transmission lines	5
2.1.1	Coplanar waveguide	7
2.1.2	Conductor-backed coplanar waveguide	8
2.1.3	Microstrip line	9
2.1.4	Planar lines	10
2.2	Filling factor	10
2.3	Scattering matrix	12
2.4	Spin system	12
2.4.1	Host crystal	12
2.4.2	Rare-earth ions	13
2.4.3	Spin dynamics	16
3	**Planar transmission line design and simulation**	**19**
3.1	Full ground plane	22
3.2	Meandering-ground line	26
4	**Fabrication methods**	**31**
4.1	Niobium thin films	31
4.2	Alignment	33
4.2.1	Membrane	33
4.2.2	Top chip	34
4.3	Limitations	35
4.3.1	Thin film fabrication	36
4.3.2	Membrane placement and alignment	37
4.3.3	Top chip placement and alignment	39
4.3.4	Layer gaps	40
4.3.5	Electric connections	41

5 Power-dependent transmission spectra **43**
5.1 Measurement setup 44
5.2 Room temperature transmission 45
5.3 Cryogenic temperature 46

6 Conclusion **51**

A Transmission line parameters **53**

B Fabrication recipes and techniques **59**
B.1 Thin films 59
B.2 Membrane placement 61
B.3 Top chip alignment 61

Bibliography **63**

Acknowledgments **69**

Chapter 1

Introduction

With the gaining accuracy of measurement devices and commercially available dilution refrigerators capable of reaching temperatures close to absolute zero, researchers seek to explore the borders of the quantum realm. Different approaches have emerged to use the peculiar properties of the smallest particles and energy quanta in a technological framework. One of those is quantum computing getting increasing attention in recent years. While there are manifold approaches like trapped ions [1, 2], cold neutral atoms [3, 4] and nitrogen-vacancy centers in diamond [5, 6] to realize a viable platform, superconducting qubits make promising progress [7]. These delicate circuits carry excitations that require a highly controlled environment of millikelvin temperatures and near-zero magnetic fields. Under these conditions, coherence times are sufficient to manipulate and interact with the excitations carried by individual qubits. Their states are exchanged by photons in the microwave regime. However, the wiring of such systems puts restrictions on the scalability since multiple lines need to be fed inside the cryostat for addressing and coupling of qubits. Moreover, crosstalk as well as connection topology of densely packed qubits are subject to current research. A way of enhancing the computing power of a quantum processor without increasing the number of qubits is supplementing a quantum memory. The advantages of such hybrid quantum architecture have been investigated in various studies [8–10]. In particular, the dimensions of a planar grid qubit processor with nearest-neighbor connections can be decreased considerably when adding a storage unit to the system [11]. Capable of storing quantum states and retrieving them at a later point in time, it would serve the purpose of random access memory in a classical computer. For operation in the vicinity of the qubit processor, it should match the working conditions in terms of temperature, magnetic field and frequency described above. However, research is mostly centered on optical quantum memories [12] for quantum communication over long distances utilizing quantum repeaters [13]. Although microwave photons can be interfaced to optical frequencies, the conversion introduces an additional loss channel and is limited by the transduction efficiency [14]. A review of approaches for the implementation of quantum memories is given by Simon et al. [15].

For microwave quantum memory, rare-earth ions are attractive candidates. Their hyperfine spin states of 4f electrons shielded by 5s and 5p orbitals exhibit long coherence times [16]. Excitations can be stored in frequency or temporal multiplexed manner [17, 18]. The former could be realized by implementing an atomic frequency comb protocol into the microwave regime. The paramagnetic spins of the doped ions inside a crystal are addressed by the magnetic field component of photons propagating in micro-circuits. In many electron paramagnetic resonance (EPR) experiments, planar micro-resonators are used to address the spin ensemble [18–20]. They provide field strengths much higher than box mode cavities inside the sample, hence improving the filling factor [21]. However, their operating range is bound to the resonator's resonance frequency. An external magnetic field is then swept to tune the electron transitions onto resonance. This procedure can be applied at different frequencies by using multiple resonators to get a spectrum of EPR transitions as a function of applied field strength.

A cavity-free approach enables agile operation over a broad frequency band covering all hyperfine transitions. Therefore, the transition spectrum is accessible by mere frequency sweeps at different field strengths with only one device. By this, the versatile advantages of multifrequency EPR outlined by Misra [22] are applicable. A few of them are pointed out here:

- *Identification of relaxation mechanisms*
  To attain comprehensive knowledge about the mechanisms governing relaxation times, their temperature as well as frequency dependence must be known. In contrast to direct and thermally activated processes the spin-lattice relaxation is independent of frequency.

- *Distinction between field-dependent an field-independent processes*
  The absorption lines of a material hold contributions from various effects like the field-dependent Zeeman splitting or the field-independent hyperfine interaction. By analyzing a line at multiple frequencies, it is possible to distinguish its origins.

- *Differentiation between the spectra of multiple species*
  The absolute and relative positions of EPR lines are characteristic of different species. By observing spectra changing with fields, the species can be differentiated.

Apart from that, the broadband method also adds to the scope of pulsed EPR techniques. Protocols like the frequency comb rely heavily on addressing multiple transitions simultaneously. It is therefore favorable to utilize transmission lines exhibiting a flat transmission curve and low reflections over the frequency range spanned by the hyperfine transitions of rare-earth ions. Additionally, the microwave signal should be coupled to the spin system as efficiently as possible.

This work's purpose is to lay out a path to the fabrication of a superconducting transmission line in a planar design. First, we will look into the theory of transmission lines best suited for efficient coupling to paramagnetic impurities while opting for high transmission over a wide range of frequencies. After understanding the spin system under investigation, transmission line theory is put to application to create the layout of a superconducting micro-chip. The design choices for the conversion between the electromagnetic mode of different transmission line configurations are explained. In the following chapter, performance restrictions raised by fabrication techniques are discussed. First transmission spectra recorded with the novel transmission line design at cryogenic temperatures are provided subsequently. The outlook summarizes techniques to further investigate rare-earth ions, contributing to the controlled operation of microwave quantum memory.

Chapter 2

Theory

A profound understanding of the fundamental principles involved is essential to achieve high performance of the transmission line. For efficient transmission, the electromagnetic signal should enter and travel along the line with reflections as low as possible. The ensemble of rare-earth ions can then couple inductively to the magnetic field component of the wave. Upon excitation at a transition frequency of an ion, transmission is reduced and can be detected.

2.1 Planar transmission lines

The purpose of a transmission line is to guide the electromagnetic wave. In contrast to resonators designed for one specific frequency, transmission lines support a wide spectrum of frequencies. In microelectronics, a variety of planar transmission lines are commonly used as they can be fabricated with thin film technology on microscopic dimensions. The impedance constitutes a characteristic property of a line, which is determined by its dimensions and material properties.

The quasi-static impedance of a substrate-based planar transmission line can be calculated analytically by conformal mapping techniques. The geometry of curved field lines is transformed by a suitable mapping function to a simple case like a coaxial line or parallel plate capacitor with known analytical formulas. A general model for planar layouts is given by Simons [23]. The model consists of a flat central signal conductor of width s surrounded by parallel ground planes. Two of them enclose the signal conductor in a common plane, as shown in Figure 2.1. w describes the gap separating the signal line from the coplanar ground planes. The shielding ground planes are separated vertically by $h_{3,4}$ from the signal line. The spaces between are partially filled by dielectric substrates of relative permittivities $\varepsilon_{r1,r2}$ and thicknesses $h_{1,2}$. Characteristic impedance Z_0 and effective dielectric permittivity ε_{eff} now solely depend on these quantities.

$$Z_0 = \frac{60\pi}{\sqrt{\varepsilon_{eff}}} \left[\frac{K(k_3)}{K(k_3')} + \frac{K(k_4)}{K(k_4')} \right]^{-1} \tag{2.1}$$

$$\varepsilon_{eff} = 1 + q_1(\varepsilon_{r1} - 1) + q_2(\varepsilon_{r2} - 1) \tag{2.2}$$

where $q_{1,2}$ are the partial filling factors

$$q_{1,2} = \frac{K(k_{1,2})}{K(k_{1,2}')} \left[\frac{K(k_3)}{K(k_3')} + \frac{K(k_4)}{K(k_4')} \right]^{-1} \tag{2.3}$$

and $K(k_i)$ is the complete elliptical integral of first kind with modulus

$$k_{1,2} = \frac{\sinh(\pi s/4h_{1,2})}{\sinh(\pi(s+2w)/4h_{1,2})} \tag{2.4}$$

$$k_{3,4} = \frac{\tanh(\pi s/4h_{3,4})}{\tanh(\pi(s+2w)/4h_{3,4})} \tag{2.5}$$

$$k_i' = \sqrt{1-k_i^2}.$$

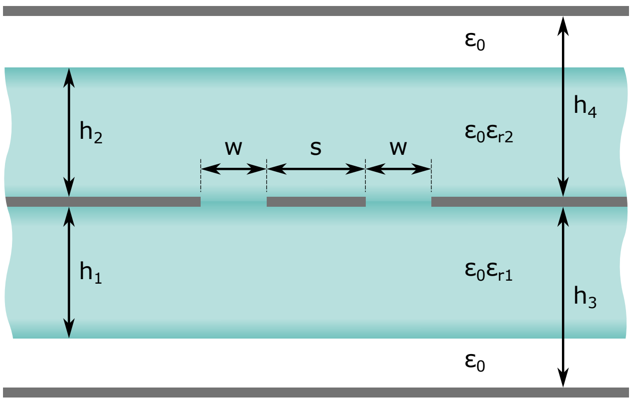

Figure 2.1: General planar transmission line model: *The coplanar signal line and ground planes are sandwiched by dielectric substrates and shielded by ground planes. Parameters in this cross section can be used to calculate properties of derived line geometries by the conformal mapping method.*

Many common transmission line types can be derived from this model such as the (sandwiched) coplanar waveguide (SCPW/CPW), microstrip line (MS) and conductor-backed coplanar waveguide (CBCPW). The expressions for impedance have proven to deliver good accuracy up to a few percent [24]. However, in this form, they still rely on simplifications rendering the conformal mapping method merely a valuable approximation of initial values for further optimization using more refined methods. The finite thickness of conductor planes as well as the thereby introduced gap between substrates are not taken into account. Furthermore, the dielectric medium is assumed to have isotropic permittivity perpendicular to the line. Beyond the scope of this thesis, there are efforts made for refining the model to cover these special cases like a correction term for the thickness of the conductors [25] and anisotropic materials [26].

2.1.1 Coplanar waveguide

The CPW is a common type of transmission line in microelectronics, especially for quantum applications. It is easy to realize because it is patterned from a single metallic layer on top of a dielectric substrate by lithography methods. The geometry can be referred to as a 2D version of the coaxial cable. But here, the flat signal conductor is shielded only on two sides by the ground planes. This leads to highly inhomogeneous field distribution around the signal line as fields are most dense in the gaps, as seen in Figure 2.2. Magnetic field lines curve around the conductor and their amplitude decays exponentially with distance from the line. The mode volume reaches inside the substrate on a length scale comparable to line dimensions [27].

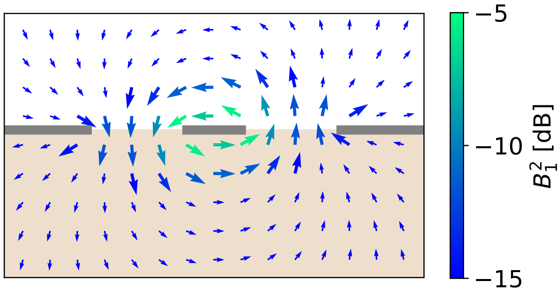

Figure 2.2: ***CPW mode:*** *The cross section visualizes magnetic field (B_1) vectors of the CPW mode on a dielectric substrate (beige). Fields are mostly concentrated in close vicinity of the signal conductor and in the coplanar gaps. Colors indicate relative power density ($\propto B_1^2$) while fields lower than -15 dB are depicted by small arrows.*

Expressions for the characteristic impedance result from Equation 2.1 for the limiting case of infinite separation of the top and bottom ground planes ($h_{3,4} \to \infty \Rightarrow k_3 = k_4 = \frac{s}{s+2w} =: k_0$) and absence of the top substrate, i.e. $\varepsilon_{r2} = 1$. The expressions simplify to

$$\varepsilon_{eff} = 1 + \frac{\varepsilon_{r1} - 1}{2} \frac{K(k_1)}{K(k_1')} \frac{K(k_0')}{K(k_0)} \tag{2.6}$$

$$Z_0 = \frac{30\pi}{\sqrt{\varepsilon_{eff}}} \frac{K(k_0')}{K(k_0)}. \tag{2.7}$$

Another variant is the SCPW with an additional substrate on top of the line. In this case, the formula for effective permittivity includes the term for the upper substrate, i.e. the definition in Equation 2.2 is used while partial filling factors are

$$q_{1,2} = \frac{1}{2}\frac{K(k_{1,2})}{K(k'_{1,2})}\frac{K(k'_0)}{K(k_0)}.$$

2.1.2 Conductor-backed coplanar waveguide

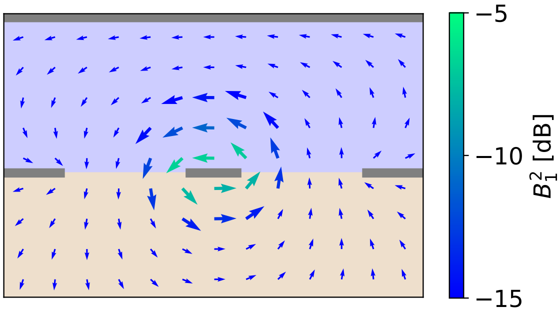

Figure 2.3: CBCPW mode: *The cross section visualizes magnetic field (B_1) vectors of the CBCPW mode. The upper dielectric substrate (light purple) is sandwiched between a CPW and a full ground plane. For increasing the coplanar gap, field distribution shifts towards the top substrate. Colors indicate relative power density ($\propto B_1^2$) while fields lower than -15 dB are depicted by small arrows.*

The CBCPW is derived from the SCPW by adding a ground plane (here: top) on the opposite side of the substrate. We allow for two substrates enclosing the coplanar conductors, as shown in Figure 2.3. CBCPW can be seen as an intermediate state between CPW and MS and will be used to transition between those line types later. As the fields are mainly allocated in the volume between signal line and ground planes, the ratio of w to h_4 determines density distribution.

The general transmission line model is simplified by setting $h_2 = h_4$ and omitting the lower ground plane ($h_3 \to \infty \Rightarrow k_3 = \frac{s}{s+2w}$). For the top ground plane in contact with the substrate, the mapping is no longer valid due to the rapid change in the boundary condition. Instead of Eq. 2.4, the expression from Ref. [28] must be used for k_2.

$$k_2 = \frac{\tanh(\pi s/4h_2)}{\tanh(\pi(s+2w)/4h_2)}$$

For large w however, the analytic results for the impedance deviate from the more accurate numeric simulation performed with CST[1]. This is assumed to be an effect of the field assumptions made for the conformal mapping breaking down in this limit. Figure 2.4 displays the deviation of the analytic formula from the simulation.

[1]For details about CST see Chapter 3.

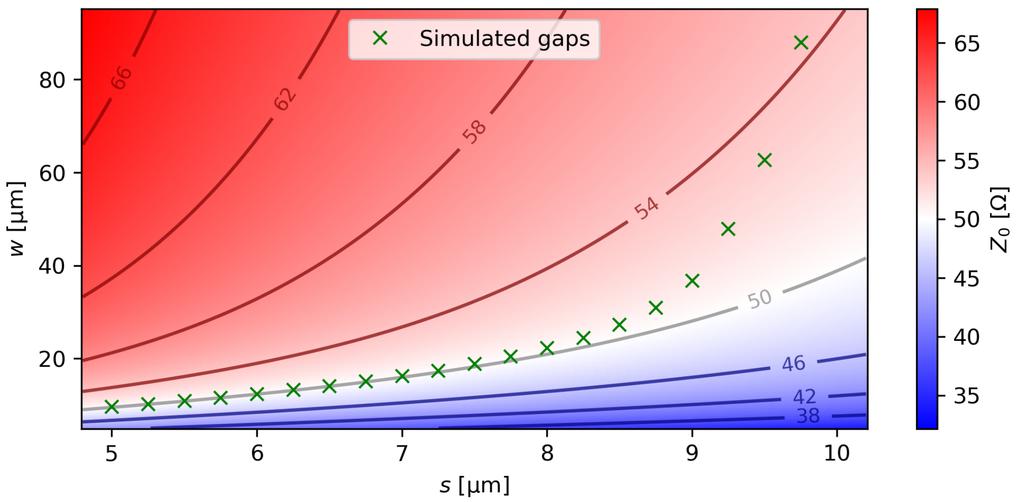

Figure 2.4: CBCPW impedance analytic vs. simulation: *The colormap indicates CBCPW impedances for $h_2 = 20\,\mu\mathrm{m}$ calculated by the conformal mapping method. When optimizing to $50\,\Omega$ using electromagnetic simulation software, w diverges when transitioning to a MS line. For $w > h_2$, analytic results deviate from the simulation.*

2.1.3 Microstrip line

The MS line consists of one full ground plane on the substrate on top of the signal line. The fields are concentrated between the conductors, hence inside the substrate, as seen in Figure 2.5. Depending on the ratio of signal width to substrate thickness, the field lines become increasingly parallel, similar to a plate capacitor.

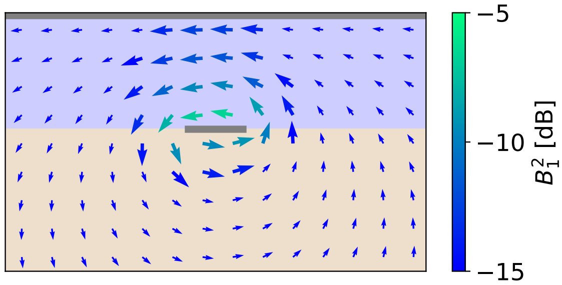

Figure 2.5: MS mode: *The cross section visualizes magnetic field (B_1) vectors of the MS mode. Fields are mostly concentrated within the top substrate sandwiched by signal line and ground plane. Colors indicate relative power density ($\propto B_1^2$) while fields lower than -15 dB are depicted by small arrows.*

The MS geometry emerges from the CBCPW for $w \to \infty$. As described above in the limiting case of CBCPW, for large gaps relative to substrate height, the conformal mapping technique does not provide reliable results anymore and electromagnetic simulation software is used to optimize impedance.

2.1.4 Planar lines

The special case of a MS line having a finite ground plane is referred to as planar lines (PL). For the ground width approaching signal width, the field distribution becomes symmetric to the horizontal plane. Particularly for wide lines as compared to substrate thickness, field lines are homogeneous and parallel between the conductors, as shown in Figure 2.6. In contrast to a coplanar geometry, a large volume of the dielectric substrate is occupied by a uniform field distribution of high power.

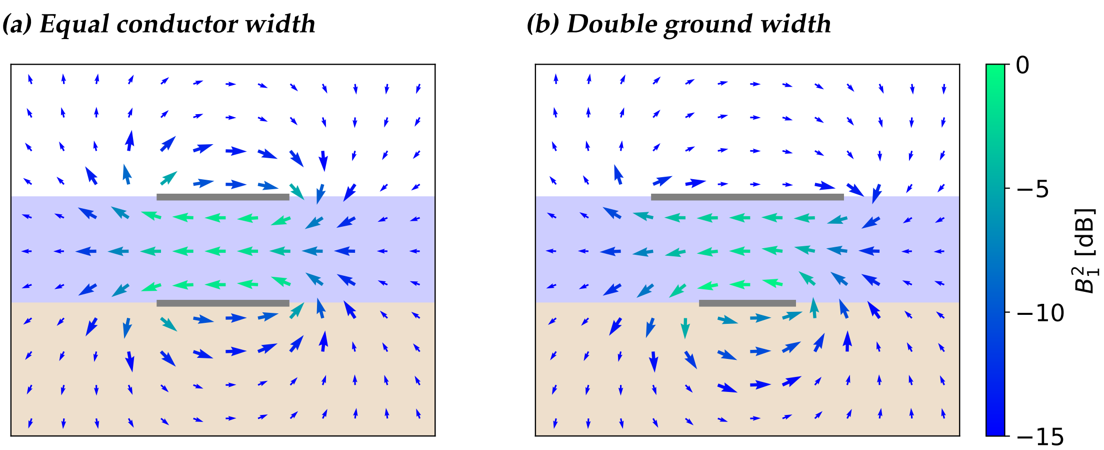

Figure 2.6: PL mode: *The cross section visualizes magnetic field (B_1) vectors of the PL mode. In the symmetric case (a), conductors have equal widths, whereas in (b), ground line has double of the width of the signal line. Fields are homogeneous in orientation and strength within the area confined by the conductors. Colors indicate relative power density ($\propto B_1^2$) while fields lower than -15 dB are depicted by small arrows.*

2.2 Filling factor

The filling factor is an important measure for effective coupling between the microwave signal and the spins. It describes the ratio of magnetic field strength H_{mw}[2] penetrating the sample volume V_S to the total mode volume V_M delivered by the conductor. The fields are integrated over both volumes to account for the field distribution of the waveguide geometry under consideration. At resonance, the EPR signal is proportional to the power absorbed by the sample, which in turn is proportional to the square of the microwave magnetic field [29]. The filling factor can therefore be calculated by

[2] Although B includes the field H generated by the conductor and the intrinsic magnetisation M of the medium ($B = \mu_0(H + M)$), in a non-magnetic substrate, B and H are equivalent up to the factor of μ_0, which is the vacuum permeability.

$$\eta = \frac{\int_V H_{\mathrm{mw}}^2 \, \mathrm{d}V_{\mathrm{S}}}{\int_V H_{\mathrm{mw}}^2 \, \mathrm{d}V_{\mathrm{M}}}. \tag{2.8}$$

In a transverse electromagnetic mode, electric and magnetic fields have no component in the direction of propagation, which is true for the waveguide geometries discussed above. At a given point in the plane perpendicular to wave propagation, absolute field amplitude oscillates in a sinusoidal manner [29]. For integration along the transmission line (e.g. the x-axis), we get a constant term that will cancel out in the calculation of the filling factor. Hence, it is sufficient to consider the ratio of fields in the perpendicular plane (yz-plane). To get an estimate on the filling factors of the line layouts under consideration, we approximate the integral by a summation over small volume elements in the plane that we can get from electromagnetic simulation.

$$\frac{\iint_{y,z} H_{yz}^2 \, \mathrm{d}V_{\mathrm{S}}}{\iint_{y,z} H_{yz}^2 \, \mathrm{d}V_{\mathrm{M}}} \rightarrow \frac{\sum_{V_{\mathrm{S}}} H_{yz}^2}{\sum_{V_{\mathrm{M}}} H_{yz}^2} \tag{2.9}$$

The filling factors for CPW, MS and PL are summarized in Table 2.1. While CPW is typically limited by 50%, line geometries where the sample is placed between the conductors reach filling factors up to 74% in the case of fully symmetric PL. This facilitates more efficient field distribution in regard to coupling to a spin ensemble.

Table 2.1: Filling factors: *Ratio of field strength distributed inside the sample to total mode volume is a measure for coupling efficiency. Line geometries sandwiching the sample between conductors yield higher filling factors. For PL, the cases of equal conductor width and ground width being double of signal width are indicated.*

	CPW	MS	PL	PL (double)
η	0.493	0.639	0.744	0.736

Evidently, the PL confine a substantial fraction of field strength between the conductors filling the sample volume homogeneously. In Chapter 2.4.3 it will become clear why this is beneficial for application in EPR experiments. The MS line being an asymmetric version of the PL provides similar field distribution but fields are more spread out within the sample volume and not as homogeneous in strength. In the case of CPW, horizontal field components are generally weaker as the strongest fields are obtained in the gaps between the signal line and ground planes contributing to a lower filling factor.

2.3 Scattering matrix

For a multi-port network, the scattering parameters indicate relations of transmitted and reflected signals. In particular, S_{ij} is determined by the ratio of the voltage V_i^- of a wave leaving a device at port i while being driven at port j with V_j^+. All other ports are terminated by a matched load. [30]

$$S_{ij} = \left.\frac{V_i^-}{V_j^+}\right|_{V_k^+=0 \text{ for } k\neq j} \tag{2.10}$$

Combining the parameters for all port combinations yields the scattering matrix. For a 2-port structure, it reads

$$\begin{pmatrix} V_1^- \\ V_2^- \end{pmatrix} = \begin{pmatrix} S_{11} & S_{12} \\ S_{21} & S_{22} \end{pmatrix} \begin{pmatrix} V_1^+ \\ V_2^+ \end{pmatrix}. \tag{2.11}$$

2.4 Spin system

Many solid-state quantum memory protocols rely on converting a photon to an excitation of defects in matter [15]. Rare-earth ions (REI) are particularly attractive for this task as their spin transitions exhibit long coherence times [16]. Optical memories exploit transitions with frequencies within the telecom C-band, where optical communication fibers exhibit the lowest loss. This is particularly interesting for applications in quantum repeaters [31] and conversion between optical and microwave photons [32, 33]. A quantum memory operating in the microwave regime exploits hyperfine transitions of the paramagnetic impurities. Close to zero magnetic fields, the hyperfine structure of REIs gives rise to transition frequencies of several GHz. Coherence times of 23 ms have been detected for Er^{3+} ions in $CaWO_4$, which is also used in this work [34].

2.4.1 Host crystal

Calcium tungstate ($CaWO_4$) is an optically transparent substrate of tetragonal crystal structure. Its orthogonal crystal axes a, b, c span the unit cell of dimensions $5.2 \times 5.2 \times 11.4\,\text{Å}^3$. The crystal structure[3] is depicted in Figure 2.7. Dielectric permittivity in the ab-plane is isotropic at $\varepsilon_{a,b} = 11.7$ whereas $\varepsilon_c = 9.5$ [37].

It renders an attractive host for long coherence times of magnetically sensitive electron spin transitions as $CaWO_4$ offers low nuclear spin density compared to other materials. Magnetic field fluctuations in the environment of the electron spin can provoke dephasing. In commonly used yttrium-based crystals, the sole

[3]Structure visualization with VESTA [35] and crystalline parameters taken from Ref. [36].

isotope of Y has nuclear spin $I = 1/2$ leading to comparably high magnetic noise in the environment of the electron. Hence, Y-based crystals can not be isotopically enriched to suppress the noise. For $CaWO_4$ however, the only nucleus with non-zero spin is an isotope of W with $I = 1/2$ at a natural abundance of 14%.

The substrates used in this work originate from a natural abundance single crystal of high purity (5N). The growth procedure is explained by Erb and Lanfranchi [38]. The Er concentration has been estimated to be $[\mathrm{Er}^{3+}] = 0.7 \pm 0.1$ ppb [34].

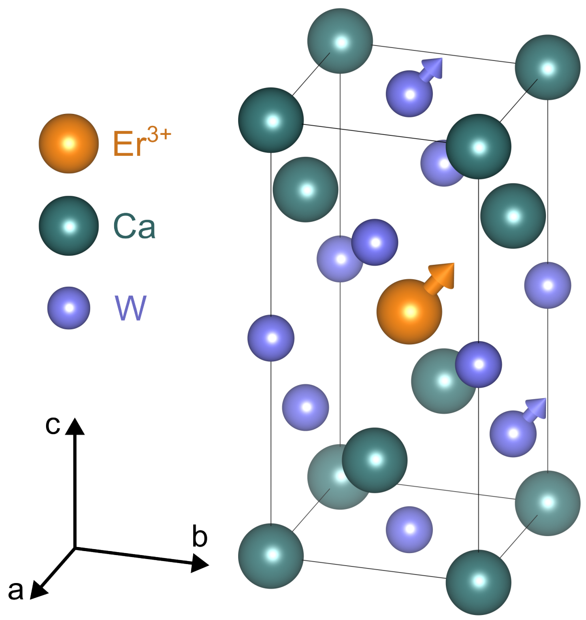

Figure 2.7: Crystal structure of Er^{3+}:$CaWO_4$: *The tetragonal unit cell exhibits an anisotropic c-axis. Er^{3+} ions substitute at the lattice site of Ca^{2+}. 14% of tungsten atoms carry a nuclear spin. Oxygen atoms are not visualized for clarity.*

2.4.2 Rare-earth ions

The set of elements with a partly filled 4f shell is known as the lanthanide series or rare-earth group. Their 4f electrons are shielded by $5s^2$ and $5p^6$ shells, enabling narrow line widths of 4f - 4f transitions. The energy level landscape of REI doped into a crystal is governed by multiple interaction mechanisms. Coming from the free ion Hamiltonian including spin-orbit coupling, states are indicated by their quantum numbers S, L and $J = L + S$, which are the spin, orbital and total angular momenta numbers, respectively. For the configuration of $4f^{11}$ electrons of Er^{3+}, the lowest energy state is denoted by $^4I_{15/2}$ using the Russel-Saunders notation $^{2S+1}L_J$. In the crystal field of the lattice, levels will split into $2J + 1$ sublevels (16 for the ground state of Er^{3+}). According to Kramers' theorem, for ions with an odd number of electrons (like Er^{3+}), these sublevels will form $J + 1/2$ doublets. The degeneracy of the doublets can only be lifted by an external magnetic field. At sufficiently low temperatures, only the lowest crystal field doublet is populated forming an effective electron spin 1/2 system.

When applying an external magnetic field, the degeneracy will be lifted, which is also known as the electronic Zeeman interaction ($\mathcal{H}_{\mathrm{EZ}}$) and the transition frequency between the states increases linearly. However, this is only true for ions without a nuclear magnetic moment. In case $I \neq 0$, the hyperfine interaction ($\mathcal{H}_{\mathrm{HF}}$) additionally splits each of the $\pm 1/2$ spin doublets into $2I+1$ hyperfine states which are only partially degenerate at zero magnetic field. These states emerge from the different combinations of nuclear and electron spin quantum numbers. At low fields, S and I are no longer good quantum numbers to describe the mixed states. The allowed transitions are not distinguishable in this regime without further knowledge. But in the high field limit in which the Zeeman interaction dominates, levels will group into two sets corresponding to quantum numbers $m_S = \pm 1/2$ for the electron spin. Each set consists of the possible projections m_I for the nuclear spin, i.e. $I, I-1, ..., -I+1, -I$. The state can then be described by $|m_S, m_I\rangle$. The selection rules give rise to a total of $2I+1$ transitions that conserve nuclear spin quantum number ($\Delta m_I = 0$).

For a full description of the system, the quadrupole interaction ($\mathcal{H}_{\mathrm{QI}}$) between nuclear spins as well as the nuclear Zeeman effect ($\mathcal{H}_{\mathrm{NZ}}$) need to be considered.

$$\mathcal{H} = \mathcal{H}_{\mathrm{EZ}} + \mathcal{H}_{\mathrm{HF}} + \mathcal{H}_{\mathrm{QI}} + \mathcal{H}_{\mathrm{NZ}} \tag{2.12}$$

Nonetheless, we only keep the critical terms for the considerations in this work and let go of the additional accuracy gained by $\mathcal{H}_{\mathrm{QI}}$ and $\mathcal{H}_{\mathrm{NZ}}$, using the reduced Hamitonian.

$$\mathcal{H} = \mu_B \mathbf{B} \cdot \mathbf{g} \cdot \mathbf{S} + \mathbf{I} \cdot \mathbf{A} \cdot \mathbf{S} \tag{2.13}$$

where μ_B is the Bohr magneton, $\mathbf{B}$ is the external magnetic field and $\mathbf{S}$ and $\mathbf{I}$ are vectors of electronic and nuclear angular momentum operators, respectively. $\mathbf{g}$ and $\mathbf{A}$ are the tensors holding g-factors for the Zeeman splitting and hyperfine coefficients, respectively.

Among erbium isotopes, only ^{167}Er carries a nuclear spin that amounts to $I = 7/2$ at a natural abundance of 23% resulting in 16 hyperfine levels for each spin $\pm 1/2$ doublet. Hence, for the remaining isotopes, namely ^{162}Er, ^{164}Er, ^{166}Er, ^{168}Er and ^{170}Er, only the first term in Equation 2.13 is applicable. Figure 2.8a summarizes the energy level splitting of the isotopes in a $CaWO_4$ crystal. The trivalent Er^{3+} ions substitute Ca^{2+} ions at their lattice site, as depicted in Figure 2.7. Their g-tensor is diagonal in the crystal frame with $g_a = g_b = 8.38$ and $g_c = 1.247$ with respect to the crystalline axes while hyperfine principle axes values of the ^{167}Er isotope are $A_\perp/h = 878\,\mathrm{MHz}$ and $A_\parallel/h = 127\,\mathrm{MHz}$, where h denotes Planck's constant [39]. Figure 2.8b shows a simulation[4] of transition frequencies of ^{167}Er:$CaWO_4$ as a function of external magnetic field.

[4] Easyspin [40].

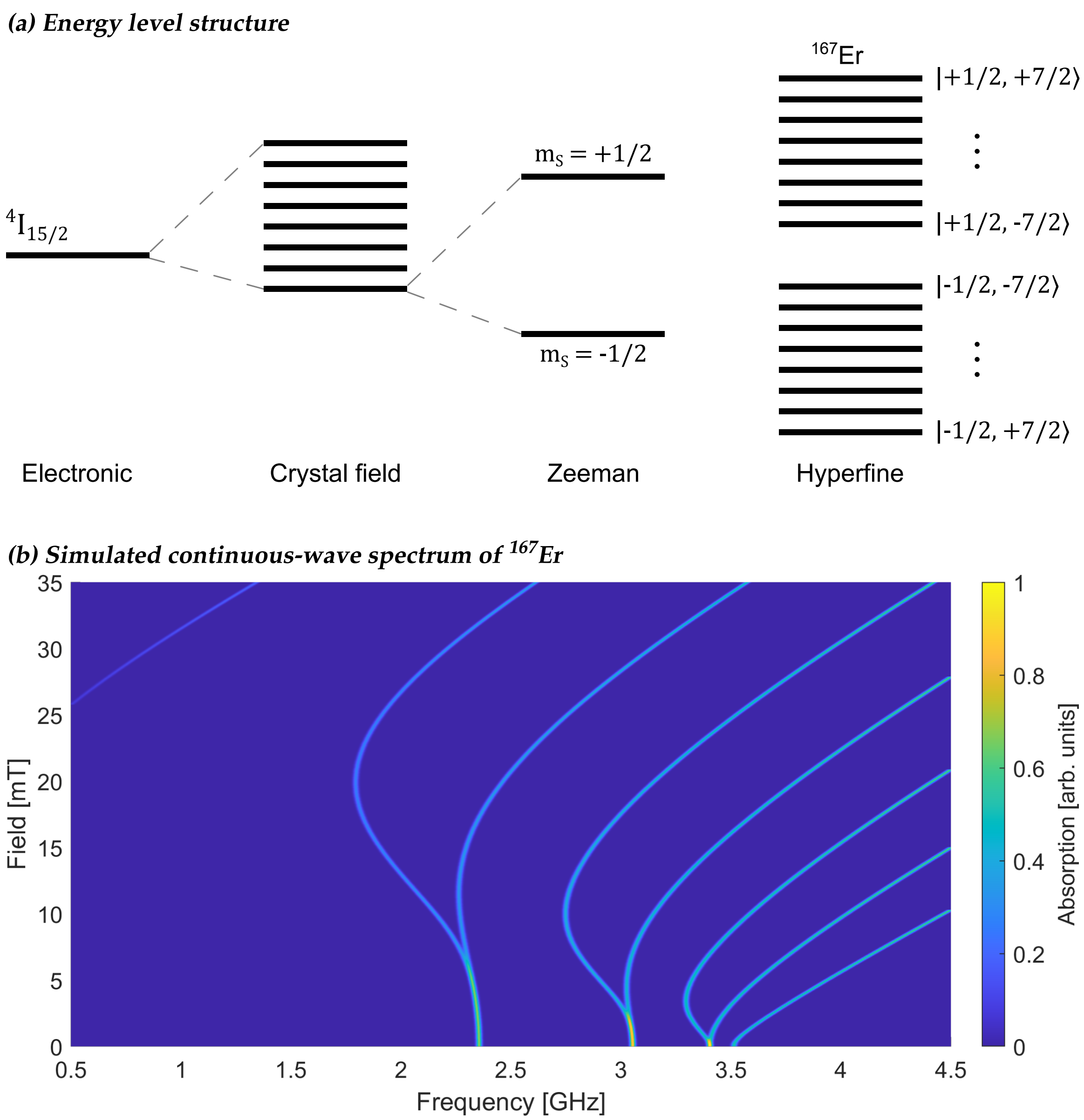

Figure 2.8: ***Er^{3+} ions in a $CaWO_4$ crystal:*** *(a) The electronic ground state splits into $J + 1/2 = 8$ Kramers doublets in the crystal field. The degeneracy of even Er isotopes is lifted by the Zeeman interaction in an external magnetic field. Due to the non-zero nuclear spin of the ^{167}Er isotope, hyperfine interaction gives rise to 16 energy levels for each spin $\pm 1/2$ doublet. In the high field limit, states can be indicated by respective quantum numbers $|m_S, m_I\rangle$ of electronic and nuclear spin. Hyperfine transitions in near-zero fields exhibit frequencies in the GHz range. (b) The hyperfine interaction due to the nuclear spin creates a splitting of transition frequencies even at zero-field. When the Zeeman interaction dominates, the slope of transition frequencies in magnetic field is dictated by the* $\mathbf{g}$*-tensor.*

2.4.3 Spin dynamics

The Bloch sphere is a convenient way of visualizing the dynamics of a two-level system. Its poles correspond to the ground ($|g\rangle$) and excited ($|e\rangle$) states, while all other points represent superpositions of the two. Rotations in the equatorial plane imply a phase φ acquired by the state. The quantum state thus can be expressed by

$$|\Psi\rangle = \cos(\theta/2)\,|g\rangle + e^{i\varphi}\sin(\theta/2)\,|e\rangle \tag{2.14}$$

using the polar angle θ, as visualized in Figure 2.9a.

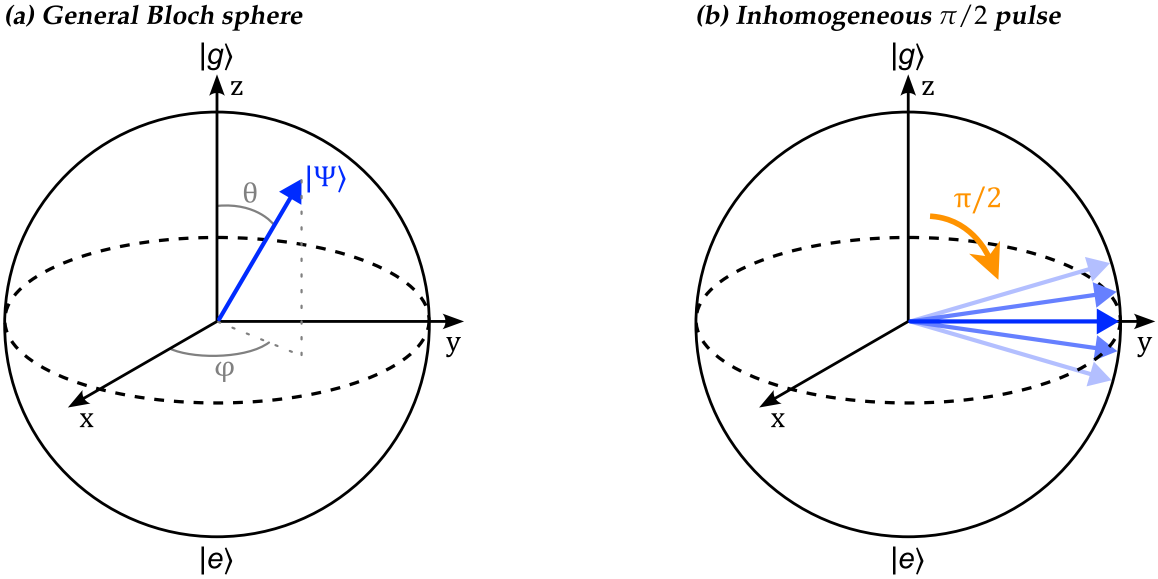

Figure 2.9: State vector in the Bloch sphere representation: *(a) The quantum state is determined by its polar and azimuthal angles φ and θ. The projection of the vector on the z-axis translates to weights of the superposition between ground ($|g\rangle$) and excited state ($|e\rangle$). The phase of the state is expressed by φ. (b) The flip angle in the representation of a spin ensemble depends on the amplitude B_1 and duration τ_p of the driving magnetic field pulse. In the case of an inhomogeneous field distribution among the ensemble, flip angles deviate and only a fraction of spins experiences a proper $\pi/2$ pulse.*

Although the hyperfine spin system under investigation comprises diverse energy levels, in a simplified picture, we can still treat a given transition of one or an ensemble of electronic spins as effective two-level systems. This allows us to represent populations of ground and excited states on a Bloch sphere. In a static external magnetic field B_0 applied along z-direction the spins will precess around the field axis with the Larmor frequency

$$\omega_L = \frac{g\mu_B B_0}{\hbar}, \tag{2.15}$$

where $\hbar$ denotes the reduced Planck constant.

Given that the resonantly oscillating field B_1 is in phase with the spin precession and is transversal to B_0, we can change to a rotating frame of reference of the spin where B_1 is static. B_1 will therefore act a torque on the magnetic moment of the electron making the state vector revolve around the x-axis (assuming $B_1 \parallel x$). This phenomenon is known as Rabi oscillation, which has a frequency of

$$\Omega_R = \frac{g\mu_B B_1}{\hbar}. \tag{2.16}$$

The flip angle can be calculated as

$$\beta = \Omega_R \tau_p, \tag{2.17}$$

where pulse length τ_p is the time over which B_1 is switched on. A detailed derivation of the equations of motion in the Bloch sphere under a driving field is given by Schweiger and Jeschke [41].

By carefully choosing τ_p and B_1, one can manipulate the state vector in a way to create an equal superposition of $|g\rangle$ and $|e\rangle$ by flipping the state vector from the ground state onto the equatorial plane, which is known as a $\pi/2$-pulse according to the polar angle traced. It is an essential ingredient to many EPR pulse sequences [41]. Dependence on B_1 also means that an inhomogeneous field distribution among the spin ensemble will lead to detuned Rabi frequencies. Subsequently, only a fraction of spins will experience the field yielding a rotation about $\pi/2$, as depicted in Figure 2.9b. For advanced pulse sequences, it is favorable to address a large subensemble to generate a strong response.

Chapter 3

Planar transmission line design and simulation

The aim of the transmission line in this work is to transfer an electromagnetic microwave signal created by a Vector Network Analyser (VNA) with the lowest possible losses over a wide range of frequencies coupled to a sample doped with electronic spins. At the interface of signal line and spin system, strong coupling is desired to drive spin transitions, which can be then investigated with the VNA by analyzing the change in amplitude and phase of the microwave signal which has passed through the sample. Besides translating excitations to the spin ensemble, for pulsed EPR protocols it is essential to retrieve photons induced by refocusing spin moments. This chapter serves as a guideline for designing a planar transmission line based on a spin-doped crystalline membrane for efficiently activating spins.

A transmission line's performance can be enhanced by several criteria. For efficient transmission, the number of dissipated photons should be minimized. To observe hyperfine transitions of the REIs, the transmission line is investigated at cryogenic temperatures close to absolute zero. In this environment, the dielectric loss tangent of the silicon wafer supporting the conductors and the $CaWO_4$ host material are reduced by orders of magnitude [42]. Additionally, the lines are fabricated from niobium being in its superconducting state below the critical temperature of 9.3 K [43]. Therefore, resistive losses of the line are highly suppressed. Besides losses, reflections deteriorate transmission properties as well. At the interfaces between two line segments of characteristic impedances Z_1 and Z_2, the reflection coefficient amounts to

$$\Gamma_{12} = \frac{Z_2 - Z_1}{Z_2 + Z_1}. \tag{3.1}$$

For this reason, transmission line dimensions are chosen to match the standard $50\,\Omega$ line impedance of cables linking VNA and the chip inside the cryostat. Regarding coupling, the choice of transmission line type plays an important role in field distribution as discussed in Chapter 2.1. To this end, MS and PL are chosen to provide beneficial homogeneity in field orientation and strength. The line dimensions are based on dielectric properties of a $CaWO_4$ crystalline membrane of 20 μm thickness to ensure high power density within the mode volume to enhance coupling even at low input powers. At the same time, the total line length is an important factor to address a large subensemble of spins inside the crystal.

To determine the line parameters, the analytic results of the impedance calculations from Chapter 2.1 serve as initial values for further optimization with full-wave electromagnetic simulation software. We use CST[1] to set transmission line dimensions to match the 50 Ω requirement for low reflection between the line segments. Within the software, one can build a 3D model and assign material properties to the components. The electromagnetic ports are defined for a signal excitation entering and leaving the structure and to keep track of performance parameters, such as impedance, transmission and reflection. In addition, a 3D field distribution can be visualized after the simulation. The solvers are based on the finite integral technique and finite element method so the model volume will be discretized to hexahedral or tetrahedral mesh cells. The software offers the option for *Adaptive Mesh Refinement* to perform separate simulation passes to ensure the accuracy of the results. The simulation starts with a coarse mesh that is still sufficient to resolve structural details of the model. In subsequent passes, the mesh will be iteratively refined in the areas of highest field density. The simulation finishes as soon as an accuracy criterion on the S-parameters is fulfilled where their magnitude deviates from the previous pass within a defined range.

Both designs of the transmission line chips (referred to as *full-ground* for MS and *meandering-ground* for PL) consist of a thin membrane being sandwiched by two dielectric substrates each coated and patterned with niobium. The superconducting metal layer is modeled as a perfect electric conductor (PEC) of thickness of 150 nm. The dielectric permittivity of the silicon substrate is adjusted to millikelvin temperatures according to the experimental results in Ref. [42]. For $CaWO_4$, $\varepsilon_{a,b} = 11.4$ and $\varepsilon_c = 9.3$ are used for the simulations. The anisotropy axis lies in the plane of the membrane and is perpendicular to the main propagation direction of the microwaves in the planar transmission lines. The surrounding space is considered a perfect vacuum. 3D models of both transmission line chips are shown in Figure 3.1. The models are modularized to evaluate and optimize each element structure individually. Dimensions for all samples and structures used within this work can be found in Appendix A.

The S-parameters are the figure of merit in our investigation of rare-earth hyperfine transitions. The design aims for high transmission in the frequency range of $1 - 8$ GHz for efficient analysis of multiple spin transitions.

[1]CST Studio Suite 2018, Dassault Systèmes.

(a) ***Full-ground*** *(Sample 11F)*

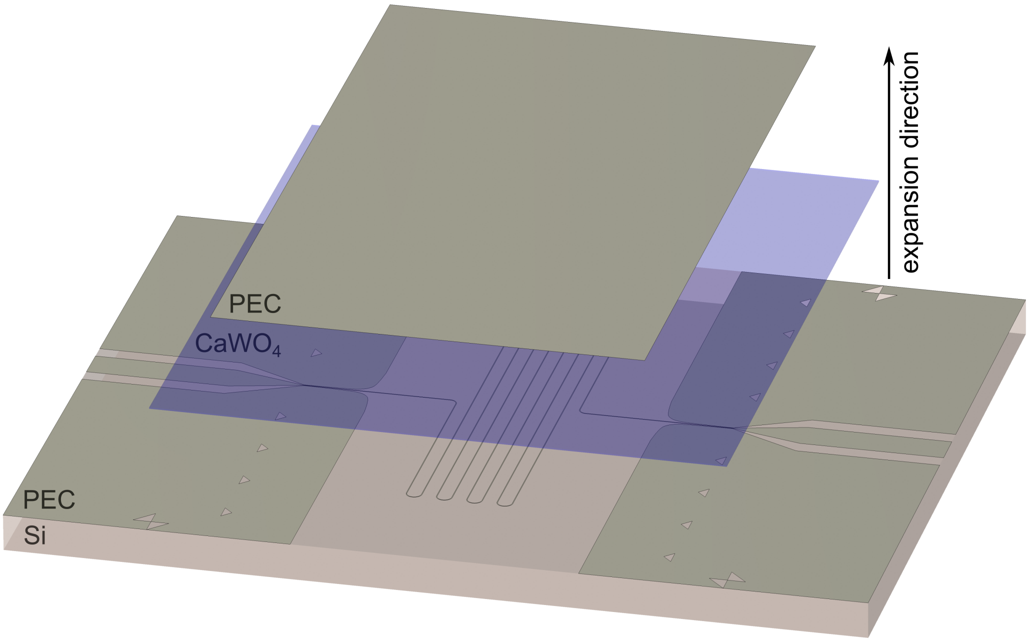

(b) ***Meandering-ground*** *(Sample 15M)*

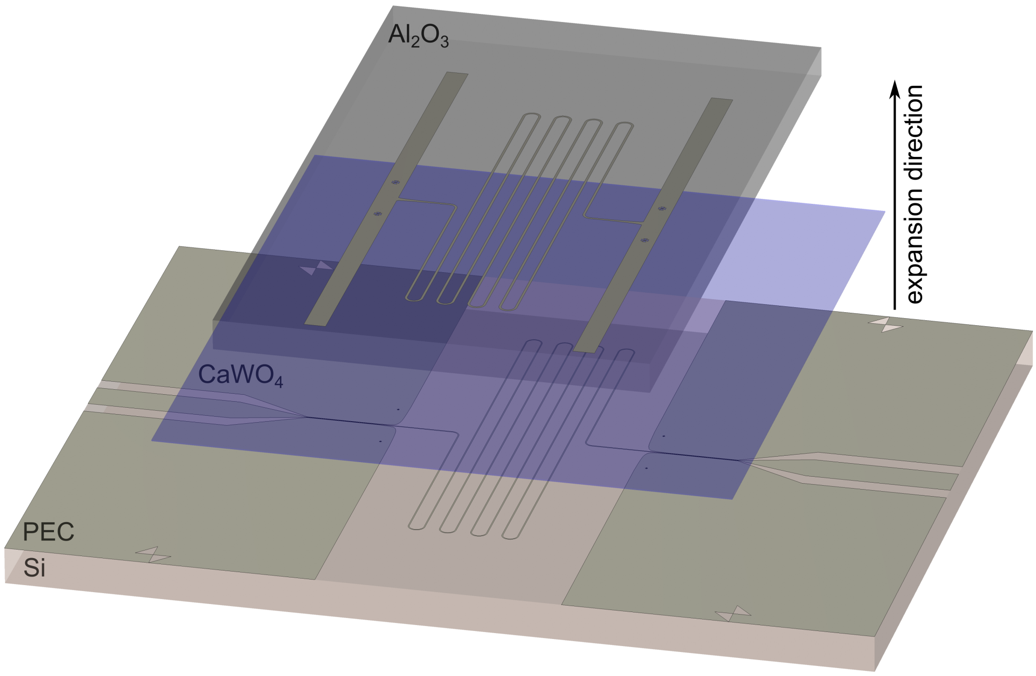

Figure 3.1: 3D models of transmission line chips: *The* $CaWO_4$ *crystal is sandwiched between substrates coated with a superconducting metal layer. The two designs feature a meandering MS (a) and meandering PL (b). For a detailed discussion on their constituents, see Chapters 3.1 and 3.2.*

3.1 Full ground plane

Since the superconducting line needs to be connected electrically to a coplanar printed circuit board (PCB) with a signal line of the width of 0.5 mm, the first structure on the chip is a taper, which reduces the larger CPW dimensions to the scale of membrane thickness. By adding the crystal, the line type changes to SCPW. A smooth transition can be achieved by overlapping the membrane with the tapering section of the line, as depicted in Figure 3.2. For the large initial dimensions, the effective permittivity and hence impedance barely change when introducing the thin membrane. Along the linear taper, the mode volume shrinks gradually until most fields are concentrated inside the crystal at the width of signal line equal to 5 µm. The simulation results are shown in Figure 3.3a.

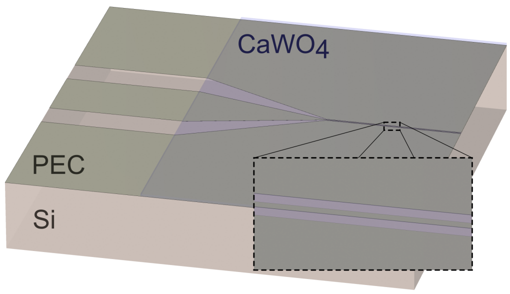

Figure 3.2: 3D model of the taper: *The linear taper transitions from CPW to SCPW dimension while smoothly introducing the membrane.*

To convert the microwave mode further, a ground plane on top of the crystal is introduced, thus creating a CBCPW. It is rather a capacitively coupled floating ground as it has no galvanic connection to the ground planes of the CPW. This conductor plane is deposited on a second silicon substrate which is facing down on the crystal. For the simulations however, the upper substrate is not considered to save time and computation power. The propagating microwave mode is fully shielded by the full layer of superconductor and, therefore, does not penetrate into the substrate, allowing to fully neglect the latter in the simulation. As a significant portion of propagating microwave fields is already confined inside the crystal within the SCPW dimensions, the additional ground plane truncates only a small fraction of the mode volume. The characteristic impedance of the line would drop to 48.7 Ω. But instead, the coplanar gap is widened by 18% to maintain an impedance of 50 Ω.

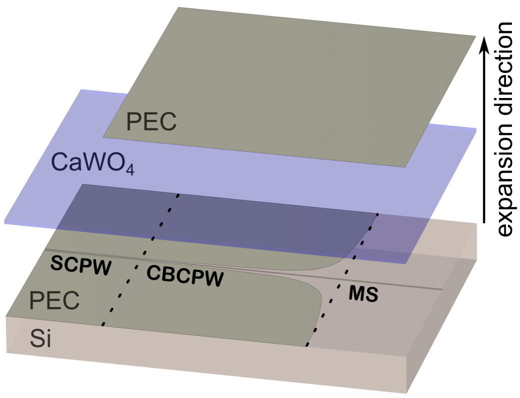

Figure 3.4: 3D model of the MS transition: *The SCPW is transformed to a MS line by introducing a top ground plane and widening the signal conductor. Coplanar gaps grow accordingly to maintain the 50 Ω criterion.*

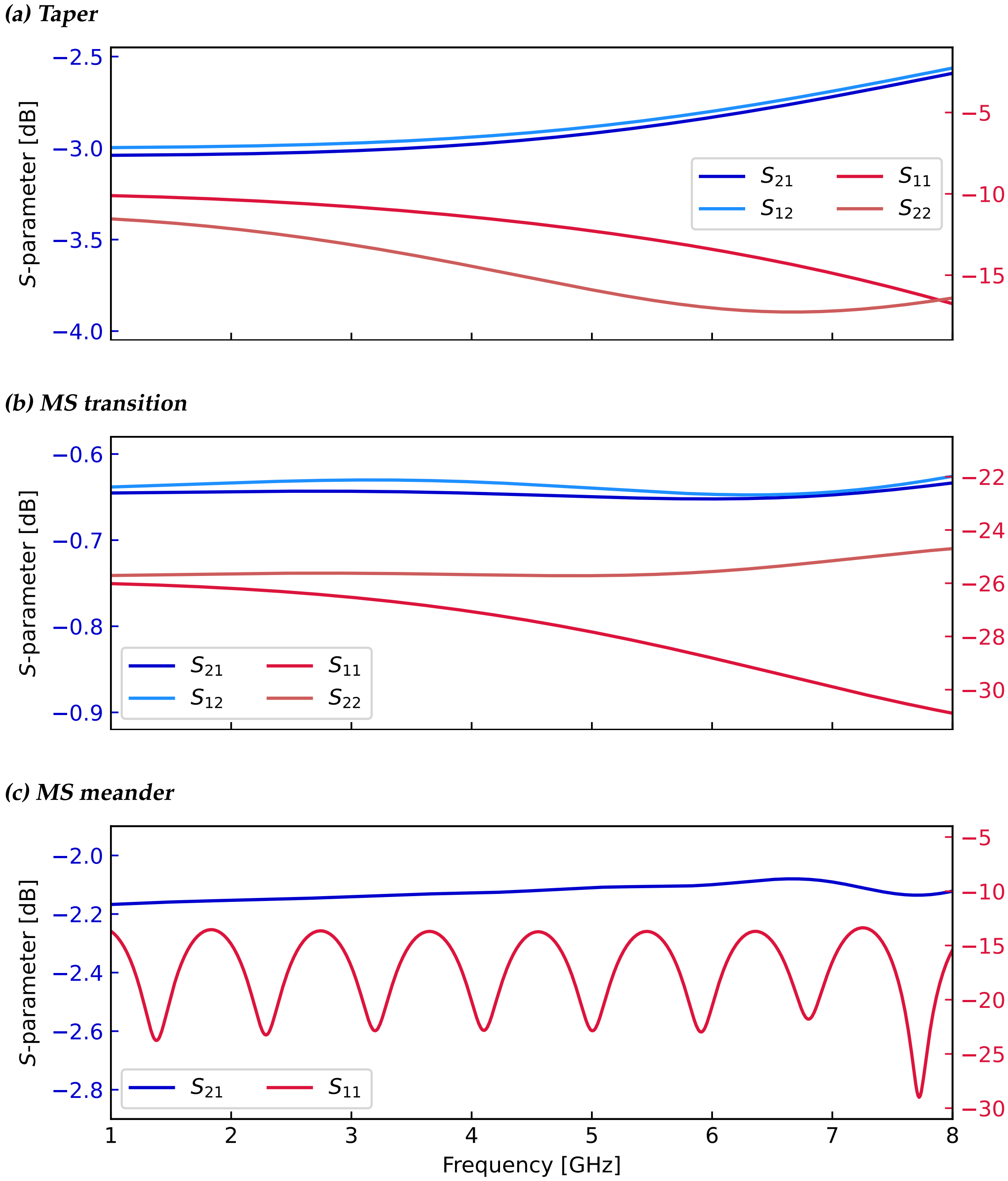

Figure 3.3: Simulation of S-parameters: *(a), (b) Transmission and reflection parameters of taper and MS transition are directional and determine the ratio of microwaves entering (S_{21}) and leaving (S_{12}) the planar transmission line. (c) Oscillations in the reflection parameter of the MS meander result from slight mismatches at the simulation ports.*

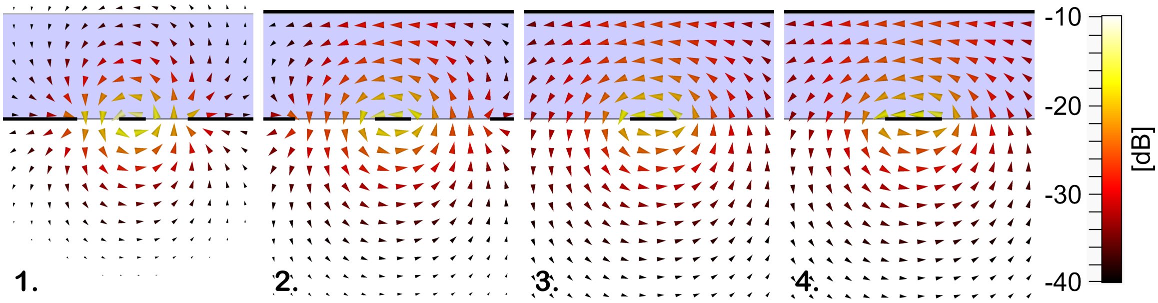

Figure 3.5: Redistribution of magnetic fields along the MS transition: *When transitioning from SCPW (1.) to MS (4.) via CBCPW (2. and 3.), highest field density shifts from the coplanar gaps to the substrate enclosed by signal conductor and top ground plane. Therefore, fields are mostly concentrated inside the crystal.*

As described in Chapter 2.1.3, the MS line can be derived from the CBCPW by extending the gaps to infinity. Here, the signal line linearly expands to the width of a MS line matched to 50 Ω. Gaps are adjusted accordingly to maintain the impedance along the transition, as seen in Figure 3.4. Figure 3.5 shows the redistribution of magnetic field component of the propagating mode from the coplanar gaps to the volume between the signal line and the top ground plane, i.e. within the crystal volume. This transition extends over a length of 1 mm. At multiple cross sections along the transition, the coplanar gaps are optimized to the respective signal width in individual simulations. The results are then interpolated to form the final shape of the SCPW to MS transition. This final design is then simulated to confirm high transmission coefficient and impedance matching (Figure 3.3b). As the structure is highly asymmetric, transmission depends on the direction of signal propagation. Concretely, S_{21} and S_{12} determine the efficiency of photons entering the MS line following the transition for interaction with the spin ensemble and receiving an excitation from it, respectively.

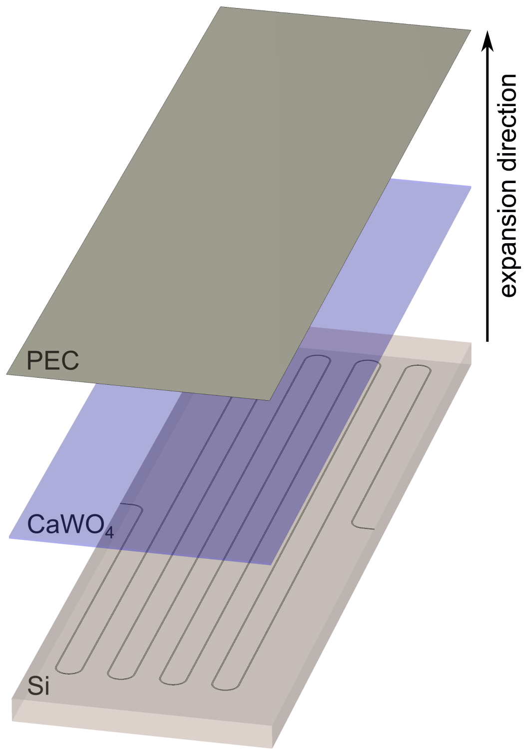

Figure 3.6: 3D model of the MS meander: *The MS transmission line is arranged in a meandering manner to increase the volume of the crystal, with which the microwave field interacts.*

In order to maximize the number of spins which are interacting with the microwave field, the signal-carrying line follows a meandering layout, as shown in Figure 3.6. By this, the lines reach total lengths of $5-10$ cm. The density of meander turns is limited by the gap between adjacent line segments. Very close positioning of the lines may lead to undesired interactions between their respective fields and distortion of the microwave mode. In a cross section of the MS line dimensions used in this work (Appendix A), the absolute field strength decays below 10% of the maximum value at a distance d of triple the signal linewidth ($d \approx 3s$) from the center of the line. Hence, we keep the distance between the meander turns wider than $2d$. The simulation results are plotted in Figure 3.3c. The oscillations in S_{11} are accounted to reflections at the simulation ports. The wavelength λ of a propagating electromagnetic wave of frequency f in a dielectric medium follows the relation

$$\lambda = \frac{v_{ph}}{f}. \tag{3.2}$$

The phase velocity v_{ph} is connected to speed of light c_0 in free space by the relative dielectric permittivity ε_r of the medium.

$$v_{ph} = \frac{c_0}{\sqrt{\varepsilon_r}} \tag{3.3}$$

For the multi-layer structure considered here, ε_r corresponds to the effective dielectric permittivity ε_{eff} of the MS waveguide. Assuming reflections occur at the simulation ports, the resonance condition is fulfilled if the total meandering

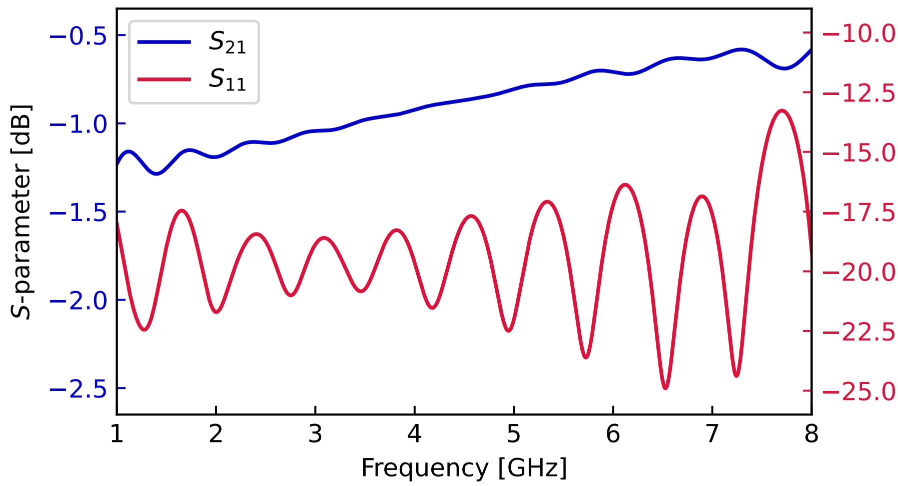

Figure 3.7: S-parameter simulation of the full-ground transmission line chip: *The complete transmission line chip exhibits high transmission and low reflections over the relevant frequency range. The scattering parameters are symmetric and normalized to an impedance of* 50 Ω *in the simulation. (Sample 11F)*

line length l matches a multiple of $\lambda/2$. Using $l = 49.2\,\mathrm{mm}$ and $\varepsilon_{eff} = 11.5$ from the simulation model, yields resonances in steps of 0.90 GHz, which is in good agreement with the frequency spacing of 0.91 GHz observed for the oscillations in the reflection parameter of the meandering line.

The chip is fully symmetric, hence, the mode is converted back to CPW to allow for transmission measurements. Figure 3.7 displays S-parameters for the full simulation of a transmission line chip (shown in Figure 3.1a) with a meandering MS line of length 51.1 mm. Transmission is beyond $-1.3\,\mathrm{dB}$ over the entire frequency range with minor fluctuations as desired. Reflections oscillate regularly like for the sole meander component but remain below a maximum value of $-13.3\,\mathrm{dB}$.

3.2 Meandering-ground line

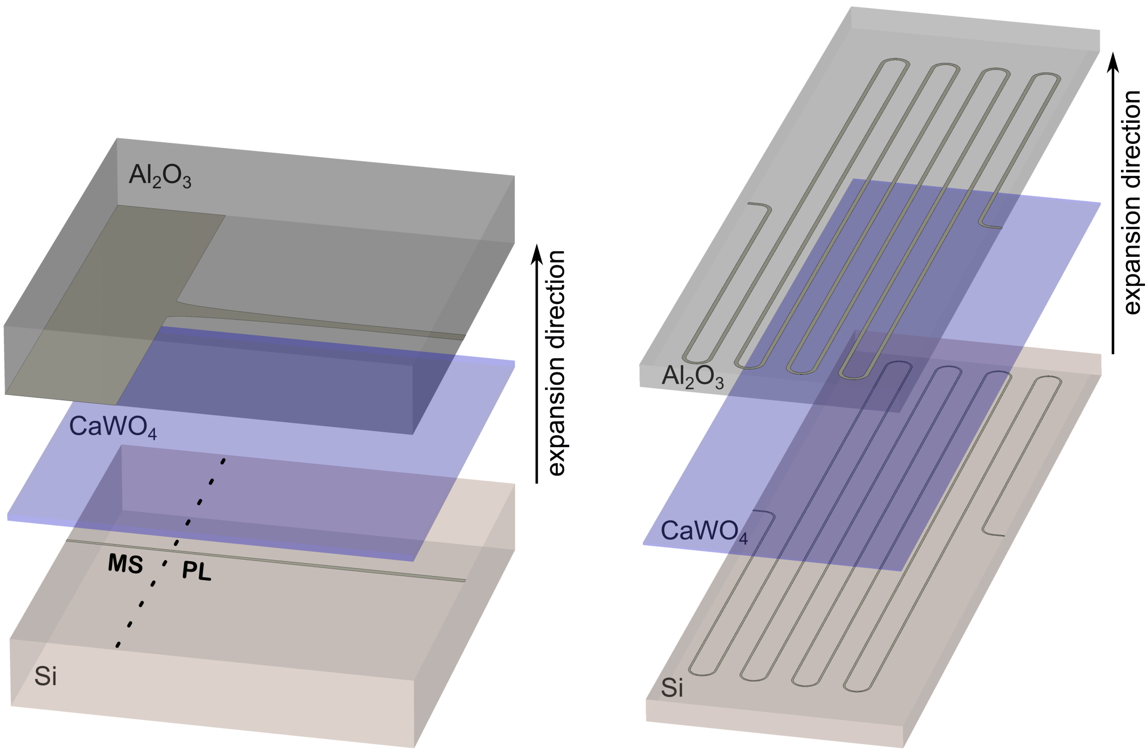

(a) Ground transition ***(b) PL meander***

Figure 3.8: 3D simulation models: *(a)The MS is transformed to PL by tapering the top ground plane down to a line while the signal conductor widens to maintain the 50 Ω criterion. (b) The PL transmission line is arranged in a meandering manner to increase the total interaction volume with the spin system.*

(a) Ground transition

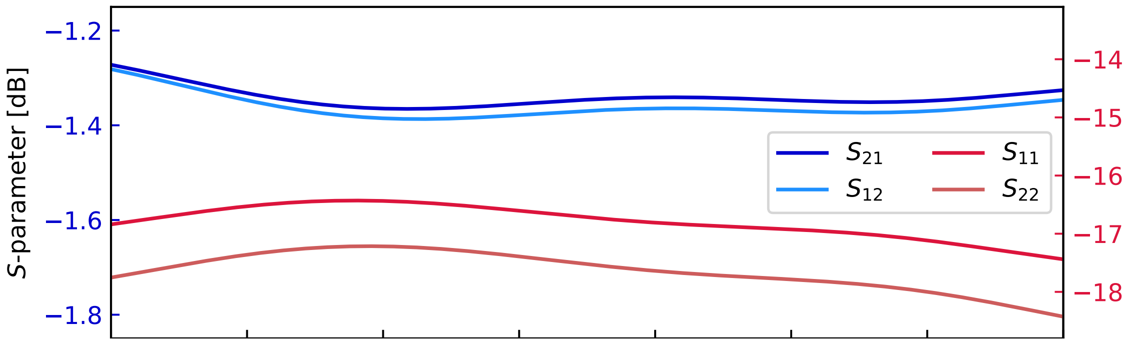

(b) PL meander

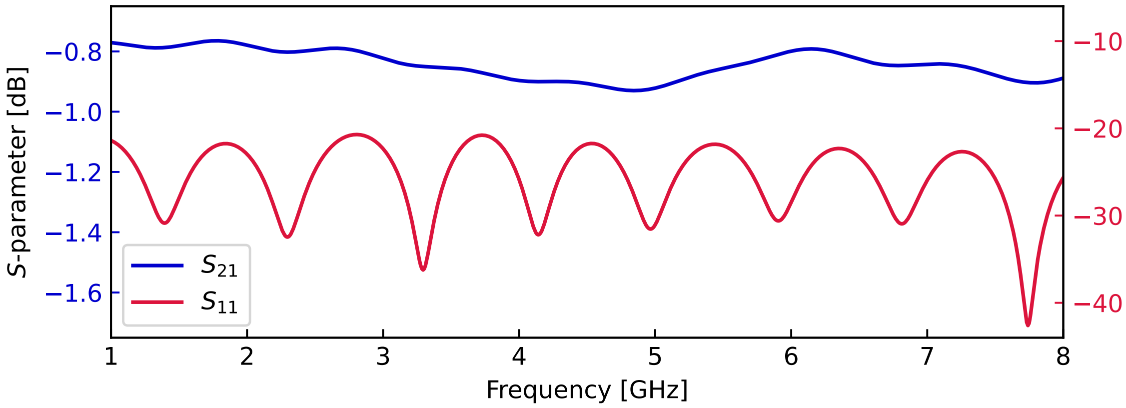

Figure 3.9: Simulation of S-parameters: *(a) Transmission and reflection are directional for transitioning from MS to PL. (b) Oscillations in the reflection parameter of the PL meander result from slight mismatches at the simulation ports.*

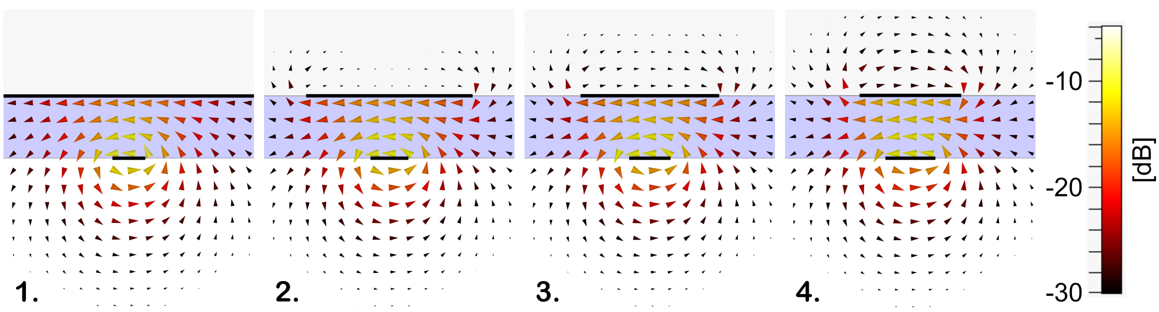

Figure 3.10: Redistribution of magnetic fields along the ground transition: *While transitioning from MS (1.) to PL (2. - 4.), highest field density further shifts inside the substrate enclosed by signal and ground conductor. Homogeneity within the enclosed area is enhanced.*

For the transmission line design utilizing the PL mode, the top chip is patterned to carry the ground line. The widths of signal and ground lines are optimized to match 50 Ω, while the ground line is around double the width of the signal line to compensate for small misalignment of the top chip in the fabrication process (see Chapter 4.3.3). For the alignment procedure explained in Chapter 4.2.2, it is necessary to fabricate the top ground line on a transparent substrate. To this end, we use *c*-plane sapphire, which is also included in the simulation since it contributes to the effective dielectric permittivity of the line.

Analogous to the full-ground design, the SCPW resulting from the taper is converted to MS. To reach PL dimensions matched to 50 Ω, signal width has to be increased from the MS. Another transition, referred to as the ground transition, follows the MS transition by linearly increasing the signal line and accordingly tapering the full ground plane on top down to form the PL geometry. Corresponding top ground widths are optimized to preserve impedance throughout the transition. The transformation of the mode from MS to PL is shown in Figure 3.10. Figure 3.9a provides simulation results for the CST model shown in Figure 3.8a.

To enlarge the interaction volume of the transmission line, we utilize a meandering line shape. For the same reasoning as described above, a minimum distance between adjacent line segments is considered. For the line dimensions under consideration (Appendix A), their spacing should be larger than $4s$. The S-parameters of the PL meander depicted in Figure 3.8b are provided in Figure 3.9b.

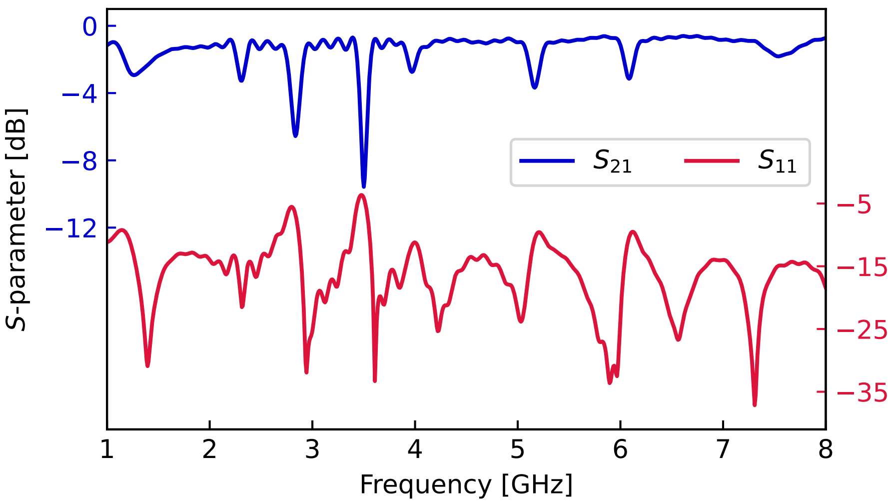

Figure 3.11: S-parameter simulation of the meandering-ground transmission line chip: *The complete transmission line chip exhibits transmission dips of irregular intensity and position in the relevant frequency range. This could be a result of numeric instabilities due to boundary conditions of the simulation. The scattering parameters are symmetric and normalized to an impedance of 50 Ω. (Sample 15F)*

Figure 3.11 displays S-parameters for the full simulation of a transmission line chip (shown in Figure 3.1b) with meandering PL of length 49.4 mm. Transmission parameters exhibit dips irregular in frequency and intensity. Reflections are comparably high and partly exceed transmission. However, it was found that the simulation results are sensitive to boundary conditions. Upon removing free space around the model and having boundaries touch the bottom and top chips, the transmission dips are largely reduced and the simulation yields a flatter response. This boundary setting continues the dielectric substrate to infinity which should not change S-parameters of the line as the boundaries are more than 400 µm from the line of dimensions of few tens of µm and microwave fields have virtually decayed to zero in this area. It is possible that the transmission dips origin from numerical instabilities. Since the simulation of the complete transmission line chip already demands most computational capacities, accuracy is limited because the simulation mesh can not be refined further to get reproducible results.

Chapter 4

Fabrication methods

As described in the previous chapter, the planar transmission line design makes use of two metallized substrates. They enclose the crystalline membrane with their coated surfaces. The layouts forming signal and ground conductors of the line are patterned using standard thin film deposition and lithography processes, as described in Ref. [44]. The assembly of all components requires special procedures for carefully handling the crystal and alignment of the top chip. As orientation and position of the top ground are critical for impedance matching and transmission amplitude, it is necessary to achieve alignment inaccuracy smaller than the line dimensions, i.e. on the order of a few micrometers. Crystal and top chip are fixed in place so the transmission line chip can be mounted in the measurement setup. All fabrication steps are conducted under controlled conditions in a cleanroom or gray room environment to avoid contamination.

4.1 Niobium thin films

The main (bottom) chip is fabricated from a high-resistivity silicon substrate. It holds not only the signal line and tapers to interface to the PCBs, but it also serves as a carrier for the crystalline membrane. The top chip will act as the ground plane on the opposite side of the crystal for the MS and as the ground line for the PL design. The top substrate is silicon in the case of the full-ground design and *c*-plane sapphire for the meandering-ground design. For precise recipes and chemicals involved, see Appendix B.

Single chips of dimensions $14.3 \times 14.3\,\mathrm{mm}^2$ are diced from a 4-inch silicon wafer of resistivity $\rho > 20\,\mathrm{k\Omega\,cm}$. In case the full wafer was not previously coated with niobium, deposition is performed on single chip level. Each chip is first cleaned thoroughly from particles and the resist layer which is applied for the wafer dicing.

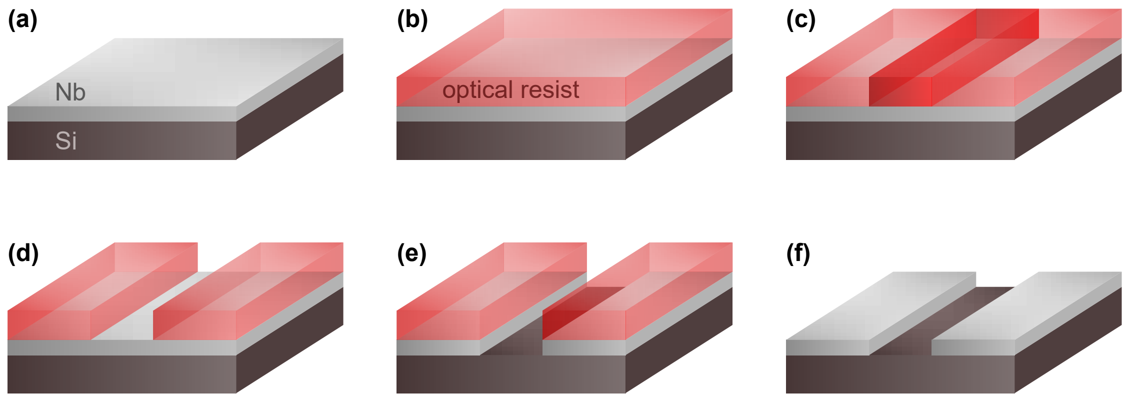

Figure 4.1: Fabrication steps for patterning superconducting chips: *(a) A thin film of niobium is deposited on a silicon substrate inside a sputtering chamber. (b) The metal is covered by a layer of optically sensitive resist. (c) The layout is written into the resist using a laser. (d) The chip is developed by chemically dissolving exposed portions of the resist layer forming a mask. (e) Exposed metal is removed by reactive-ion etching. (f) Stripping the chip from residual resist concludes the thin film fabrication.*

Niobium sputtering is executed in an ultra-high vacuum system[1]. Gaseous argon ions in the vicinity of a niobium target are ionized by a potential. The niobium atoms are then ejected from the target by the argon-ion plasma and bind to the surface of the substrate. Rotation of the mounting stage ensures the formation of a uniform layer. The deposition parameters are chosen to create a thin film of thickness 150 nm. For the lithography steps, a layer of photo-sensitive resist is applied using a spin coater. To evaporate solvents, the chip is baked on a hot plate. A laser writer[2] scans the substrate and exposes areas according to the layout written. Under illumination of the laser, the resist changes chemical composition to later create an etch mask on top of the metal layer. Homogeneity of the resist layer is critical for the laser to keep focus during the writing step. It is to note that close to the chip's edges a thick resist wall forms, which can not be written so the layout can not cover the entire substrate. Instead, a distance of about 1 mm is kept from each edge. When using positive resist, exposed areas become soluble to a chemical developer, while for negative resist, exposed areas become resistant. In the development step, the respective portion of the resist is dissolved to expose the metal while leaving the resist mask intact. The bare metal can then be removed via reactive-ion etching[3] with SF_6 gas. The resist mask protects the underlying metal from the reaction. The chip is finally cleaned by chemically stripping the residual resist leaving the patterned chip ready for further fabrication steps. All steps for

[1] Plassys.
[2] Laserwriter 200 from 4PICO.
[3] Plasmalab 80 from Oxford Instruments.

patterning a silicon substrate using positive resist are summarized in Figure 4.1.

For the main chip of the transmission line, we fabricate the layout on a $14.3 \times 14.3\,\mathrm{mm}^2$ silicon substrate using a positive resist. Afterward, the chip is cut in a wafer dicer to $12 \times 9.5\,\mathrm{mm}^2$ to remove the areas with the resist walls. This way, the taper patches are located right at the edges of the chip, which allows for short bond wires for electrical connection. The full-ground top chip is cut to $6 \times 10\,\mathrm{mm}^2$ from a metallized wafer and does not need further fabrication steps. For the top chip of the meandering-ground design, however, it is crucial for the alignment process to fabricate the structures on a transparent sapphire substrate. Using negative resist leaves the substrate edges free from metal without dicing. This way the top ground planes of both MS transitions are only connected by the ground line.

4.2 Alignment

As the transmission line structures are on the length scale of a few micrometers, alignment of the structures is crucial for the quality of the sample. To fix membrane and top chip on the bottom chip, we use GE Varnish, which is a type of varnish with good thermal conductivity at cryogenic temperatures. Due to its low viscosity, for application on the fragile structures of the transmission line chip, GE Varnish is dissolved in ethanol p.a. until a diluted yellow liquid emerges. In this form, the glue can be applied conveniently with a fine brush without acting too much force on the membrane causing it to break. Upon application, the ethanol evaporates after a few seconds to leave behind a thin film of varnish. It is important to apply the glue only to the edges of membrane and top chip to keep their interfaces clean. The varnish is left to dry for several hours between fabrication steps.

4.2.1 Membrane

The crystal was grown by A. Erb at the Walther-Meissner-Institute[4] and polished to a thin membrane by M. Stanger in the crystal and material laboratory[5] of the Technical University of Munich. A thin slab with base dimensions $8 \times 9\,\mathrm{mm}^2$ is cut from the bulk $CaWO_4$ crystal and first polished on one side. This side is then attached to a glass plate using thermoplastic glue. That way, the other side can be polished down to the desired thickness of $20\,\mu\mathrm{m}$. To reduce handling steps involving the membrane, it is directly dissolved onto the bottom chip by placing the glass plate on top of the chip with the membrane facing down. For the exact dissolving procedure, see Appendix B.

[4] `https://www.wmi.badw.de/home`, last visited 04/05/23.

[5] `https://einrichtungen.ph.nat.tum.de//kristallabor/`, last visited 03/11/23.

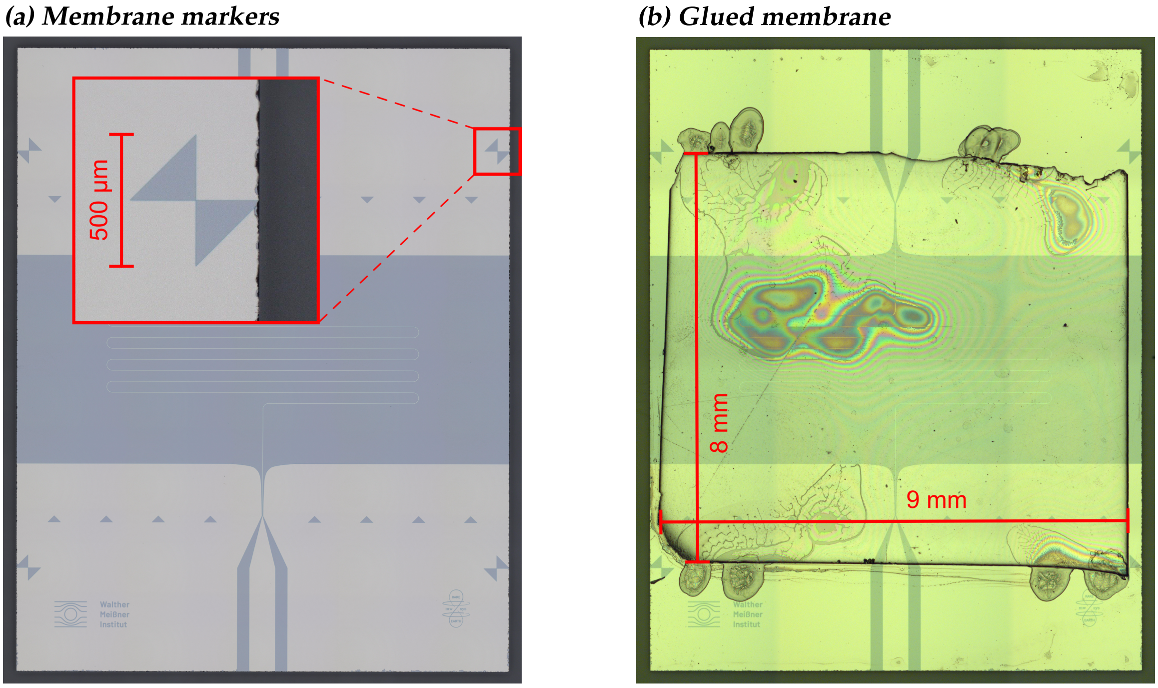

Figure 4.2: Membrane alignment: *Images taken with different microscopes. (a) Four large markers written into the bottom chip layout indicate the positions of the membrane's corners. (b) GE Varnish is applied at the edge of the membrane to keep the interface to the top chip clean. (Sample 11F)*

In the last step of ungluing, when the chip is still covered with isopropanol, the membrane can be moved using a fine brush. For alignment, the layout written in the bottom chip includes four markers for the corners of the membrane (Figure 4.2a). The use of a microscope or magnifying glass is convenient for checking the position of the membrane. The markers only serve as guidance as an exact alignment is impossible due to imperfections in the shape of the membrane. However, for reasons explained in Chapter 3.1, the taper tolerates slight misalignments of the membrane's edge at the large CPW dimensions.

After drying off the chip, GE Varnish is applied at the edges facing the tapers while not covering more than 1 mm of the crystal, as shown in Figure 4.2b. Otherwise, the interface between membrane and top chip will be disrupted by the glue leading to a gap between the layers.

4.2.2 Top chip

The position of the top chip is essential for the transmission line geometry and therefore requires a procedure capable of angular and translational precision on the order of a few micrometers. Also, the top chip has to stay fixed while applying the varnish. Alignment of the top chip is performed with an optical microscope with a translation table used for horizontal shifts. While the bottom chip with glued crystal lays in the focal point on the table of the microscope, the top chip is clamped by tweezers mounted on a vertical translation stage for controllable lowering onto the crystal. Angular alignment is achieved by placing the bottom chip on a microscope slide that can be rotated by hand with sufficient accuracy. The setup is shown in Figure 4.3. Details on the alignment procedure are described in Appendix B.

The triangular markers for the full-ground top chip are shown in Figure 4.4a. They are located at the beginning of each MS transition where the top ground plane is introduced. Their tips trace the position for the edge of the fully coated silicon substrate, as shown in Figure 4.4b. For the meandering-ground design, both bottom and top chips feature cross-shaped markers patterned into their metal layers (Figures 4.5a and 4.5b). The sapphire substrate used for the top chip allows seeing the markers with an optical microscope. In addition, the markers on the top chip are large enough to see those of the bottom chip. The chips are aligned when centers of respective pairs of crosses coincide, as shown in Figure 4.5c. The alignment procedure described above is sufficient to achieve accuracy smaller than line dimensions. Hence, signal and ground conductor are correctly arranged for the PL geometry. After successful alignment, the top chip is glued to the membrane with GE Varnish.

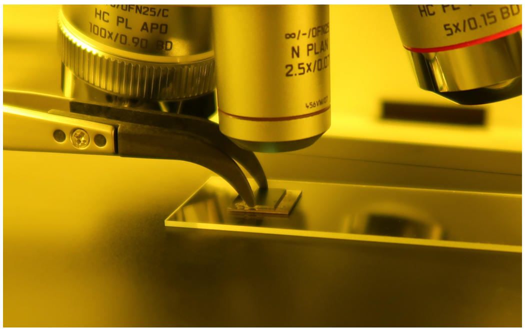

Figure 4.3: Setup for top chip alignment: *The top chip is clamped by tweezers mounted on a vertical translation stage for controlled placement. Turning the microscope slide with the bottom chip lying on top accounts for rotational alignment. Horizontal movement is managed by the translation table of the microscope.*

4.3 Limitations

The simulations in Chapter 3 assume ideal conditions for materials, structure layout and alignment. However, fabrication of the chips puts restrictions on the performance and will consequently deviate from simulated results. The most important effects to consider along the fabrication steps are discussed here. Mostly, defects lead to discrepancies in impedance, which in turn causes reflections at unmatched interfaces. Additionally, imperfections in material composition and electric connections in the setup play a role in signal loss along the transmission line.

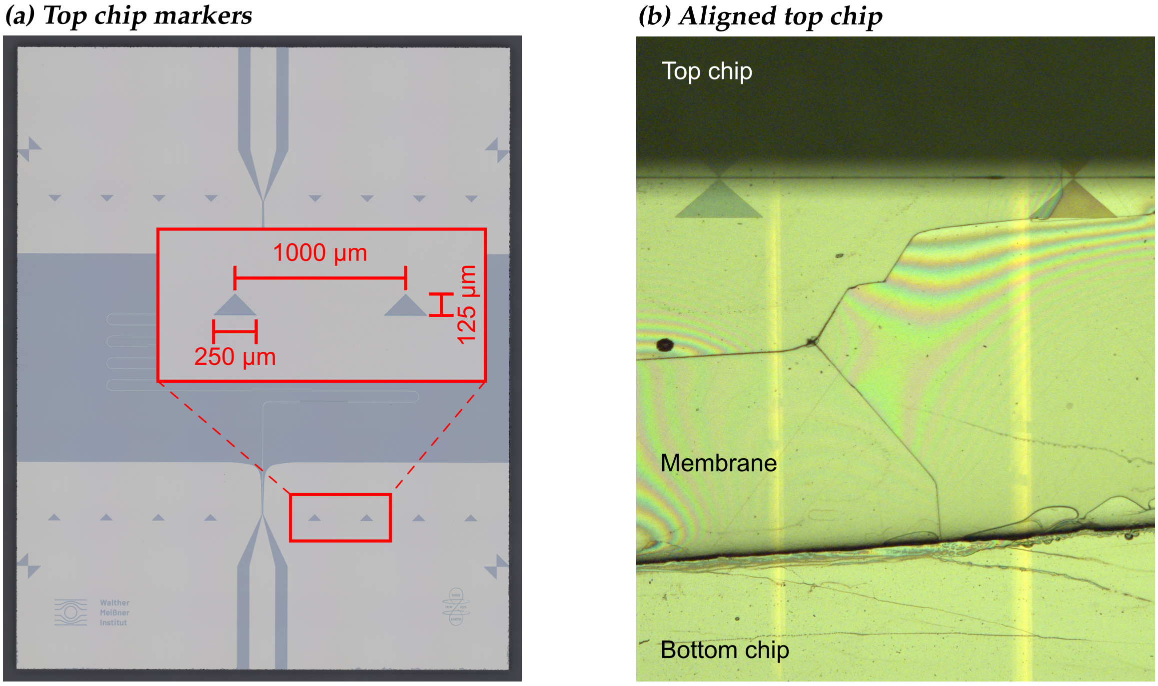

Figure 4.4: Full-ground top chip alignment: *Images taken with different microscopes. (a) Triangular markers written into the bottom chip layout trace the position of the top chip edge. (Sample 11F) (b) With the bottom edge of the top chip within focus, it is aligned to the tips of the markers. Reflections of the markers are visible on the side of the top chip. (Sample 09F)*

4.3.1 Thin film fabrication

For the fabrication of structures on the micrometer scale, cleanliness is essential throughout the steps. During spin coating, particles may obstruct the formation of a homogeneous resist layer and lead to shadow artifacts. Holes in the resist layer will get etched even without laser exposure. Furthermore, dust particles lead to a loss of focus in the laser writing step. Results can be shifts in layout, line discontinuities or interruptions in exposure. These defects disrupt the signal line, leave residual metal patches or short the line to ground (Figure 4.6). For the sapphire substrate, a negative resist is used, i.e. after lithography all unexposed resist is removed chemically. However, the development step is not yet optimized to fully remove the thick resist walls along the edges of the chip completely before affecting exposed structures. Consequently, in the corners, small patches of metal remain after etching. To avoid effects on patterned structures, this should be considered in the layout generation.

(a) Markers on bottom chip

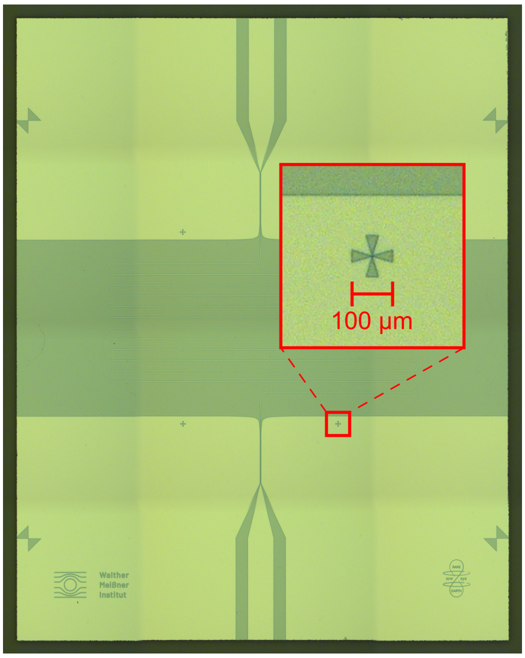

(b) Markers on top chip

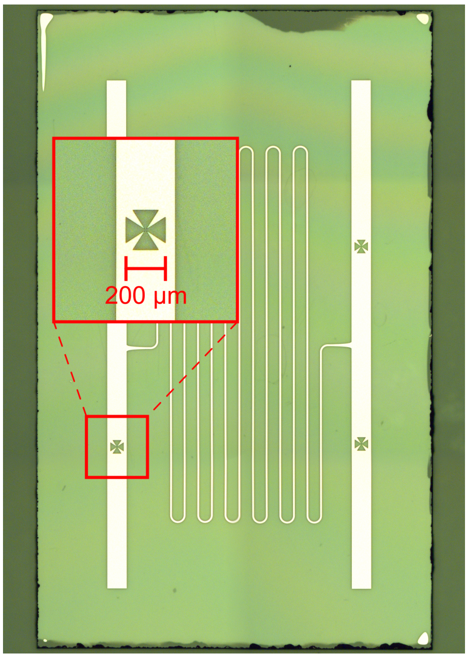

(c) Aligned top chip

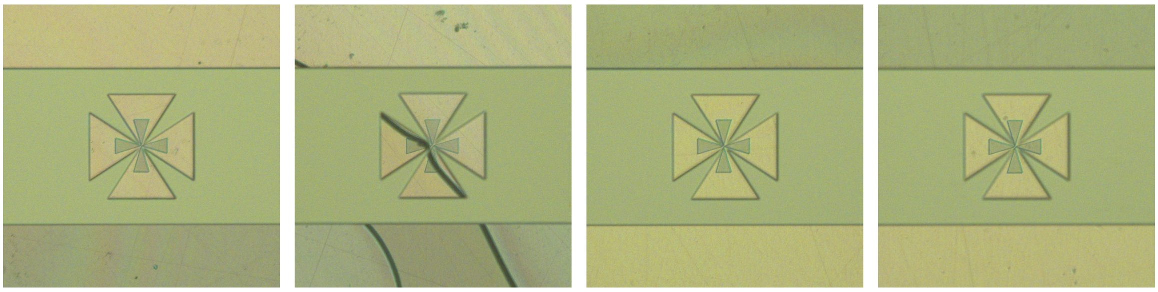

Figure 4.5: Meandering-ground top chip alignment: *Cross-shaped markers on bottom (a) and top chip (b) are centered on top of each other to align the signal and ground conductors of the line. (c) The transparent sapphire substrate used for the top chip and the larger cross dimensions allow seeing through to markers on the bottom chip. The procedure yields good alignment on all marker pairs. (Sample 16M)*

4.3.2 Membrane placement and alignment

Due to their large dimensions and small thicknesses, the membranes are prone to break during handling and alignment procedures. In fact, most membranes provided for this project had visible cracks, as seen in Figure 4.7a. Upon solving from the glass plate, they break into pieces outlines by the cracks. Separations in crystal act as defects for the transmission line where the impedance is unmatched

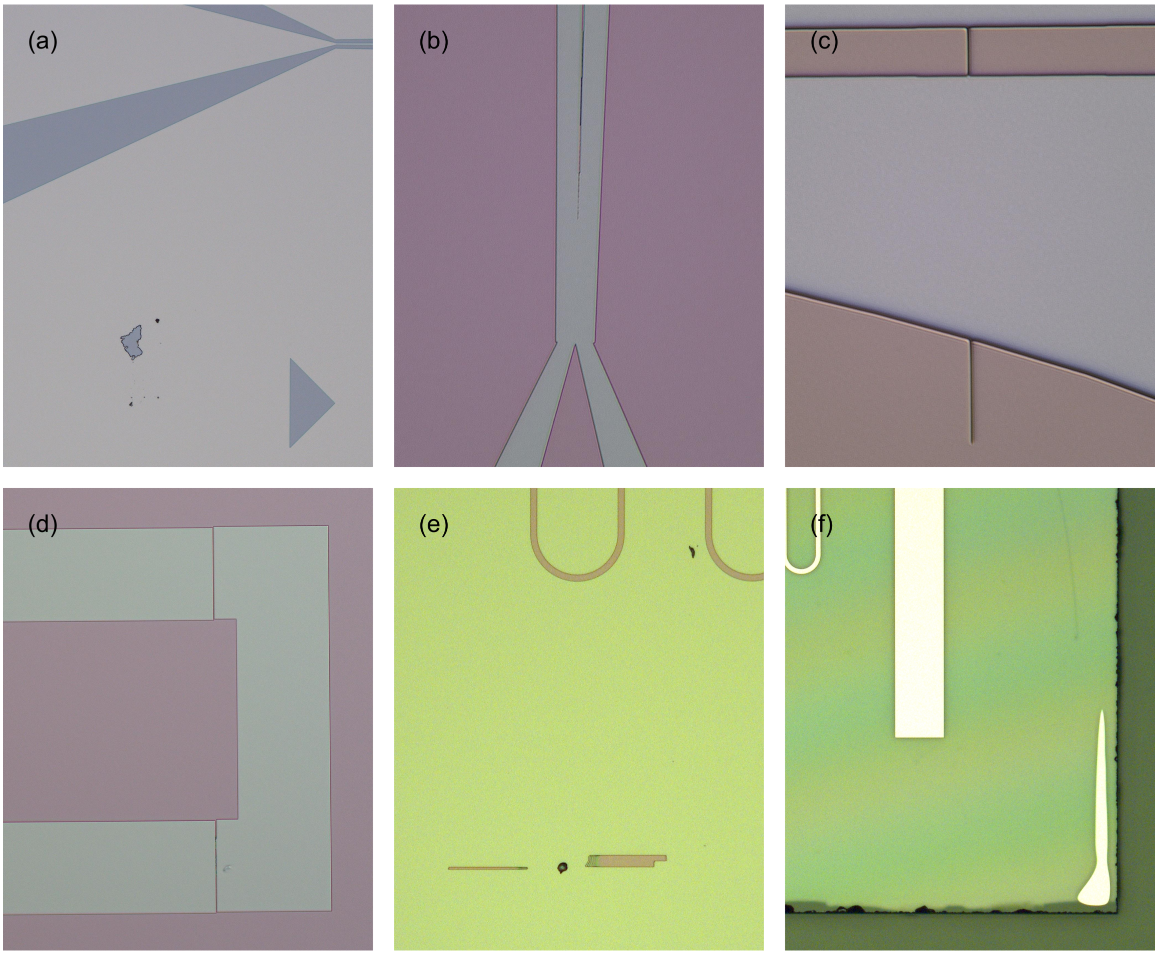

Figure 4.6: Defects in thin film fabrication: *(a) Inhomogeneous resist layer: Dust particles deposited during spin coating obstruct the shielding resist layer. Consequently, affected areas are etched and leave behind holes in the niobium layer. (b) Layout shift: An error in the laser writing process led to a shift in layout. The resist mask for the signal line is cut off at the taper after development. (c) Line discontinuity: Overexposure in one scanning cycle of the laser cuts the resist mask. After etching, the signal line (top) is potentially separated. (d) Short: A shift of the laser or interrupted exposure leaves a thin band connecting the taper patch with the surrounding ground planes, effectively shorting the line. (e) Interrupted exposure: A particle causes loss of focus and the writing process is disrupted. Small patches of metal will remain after etching. (f) Resist wall: At the corners of the substrate, the thick resist walls are not dissolved completely by the developer. Small metal patches are preserved during etching.*

since effective dielectric permittivity is altered (Figure 4.7b). Moreover, inclusions of impurities in the thermoplastic glue used to attach the membranes to their glass plates puts a major constraint on fabrication cleanliness. As the polishing and gluing are not performed in a cleanroom environment, particles are embedded in the glue. When dissolving, particles are released and contaminate the chip.

(a) Cracked membrane ***(b) Broken membrane***

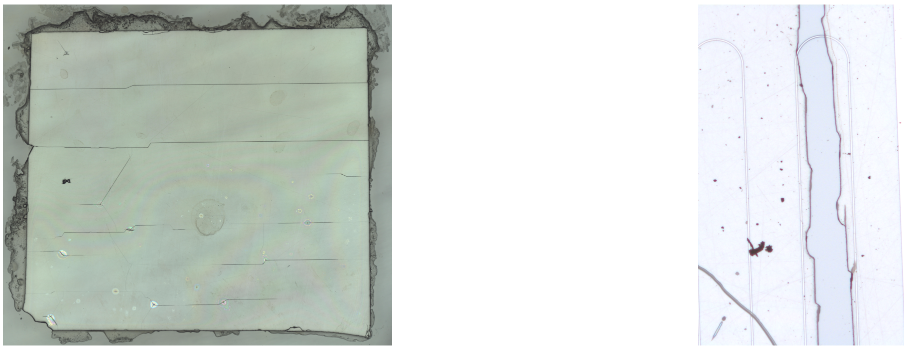

Figure 4.7: Cracked and broken membrane: *(a) Membranes exhibit cracks as they are glued to the glass plate they are polished on. When dissolving the glue, the membrane will break along the cracks. (b) Separation of membrane pieces creates defects of mismatched impedances among the transmission line, which leads to reflections of the transmitted signal. Particle inclusions from the dissolved glue pollute the chip.*

4.3.3 Top chip placement and alignment

The alignment of the top chip is an important factor for transmission as it directly affects the geometry of the planar line. Generally, the MS design is less sensitive to top chip alignment than PL. At the beginning of the MS transition, where the top ground is first introduced, CBCPW gaps are similar to that of the SCPW. Therefore misalignment by a few micrometers is tolerated by the design without

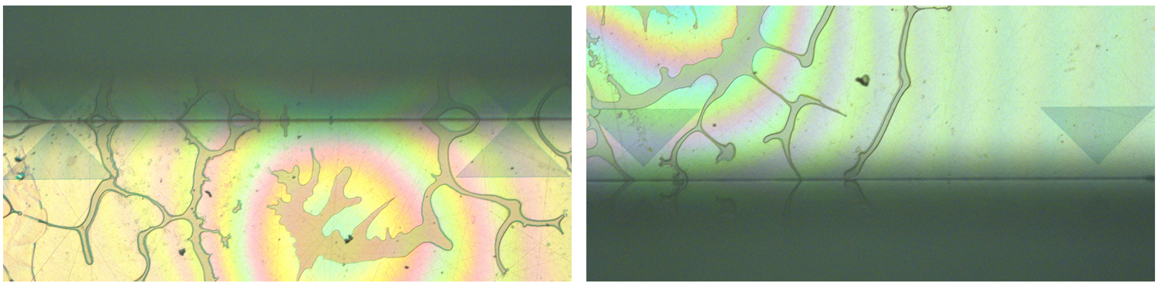

Figure 4.8: Full-ground top chip misalignment: *Due to a discrepancy of top chip length and marker spacing, only one side is aligned properly (left), while the other one is misaligned by tens of μm.*

major deviations in impedance. In fact, there is a discrepancy between the 6 mm edge length of the full-ground top chip and the 6 mm spacing between top chip markers. Alignment to one MS transition creates a shift of a few tens of µm at the other one, as seen in Figure 4.8. Since the entire meandering signal line is covered by one ground plane, also rotational alignment is not a limiting factor of the design. For a structured top chip however, translational and rotational alignment is crucial. A ground line of double the signal width provides tolerance for small deviations. Constant impedance along the transmission line requires the top ground line to follow the signal line without shifts. Not only do misaligned conductors affect impedance, but also the homogeneous field distribution of the PL mode is increasingly distorted as field density shifts towards the edges of the conductors, as simulated in Figure 4.9.

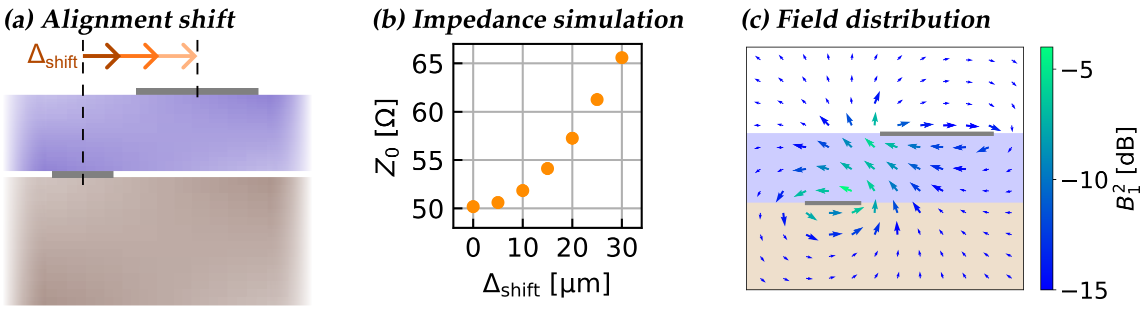

Figure 4.9: Meandering-ground top chip misalignment: *(a) For a misaligned top chip the ground conductor is shifted with respect to the signal line by Δ_{shift} (b) Characteristic line impedance Z_0 increases with Δ_{shift}. Interfaces with impedance mismatch cause reflections of the propagating signal. (c) The distribution of microwave field B_1 is increasingly inhomogeneous and distorted from the PL mode. Colors indicate relative power density ($\propto B_1^2$) while fields lower than -15 dB are depicted by small arrows.*

4.3.4 Layer gaps

Dimensions of the planar transmission lines are optimized for direct contact of the membrane to both metal layers on the chips. During fabrication however, multiple factors may introduce gaps between layers. As seen in Figure 4.7, the thermoplastic membrane glue contains impurities that pollute the interfaces. Particle size mostly ranges within several micrometers and hence they cause a spacing on the scale of crystal thickness. Moreover, two pieces of a broken membrane can overlap at the boundary effectively doubling the distance between top and bottom conductors. Especially small shards breaking from the edges may get trapped under a larger piece of the membrane while dissolving the crystal from its glass plate. Lastly, uneven pressure applied while placing the top chip opens small cavities for dissolved GE Varnish to enter the layer interfaces. Apart from a reduced filling factor, this causes a distortion of waveguide geometry. Layer gaps are simulated in CST to get an estimate for the effect on impedance (Figure 4.10). Even for spacing of a few µm at interfaces, impedance strongly increases. This leads to the assumption, that layer gaps might be one of the major restrictions on fabrication quality.

(a) Interface spacing ***(b) Impedance simulation***

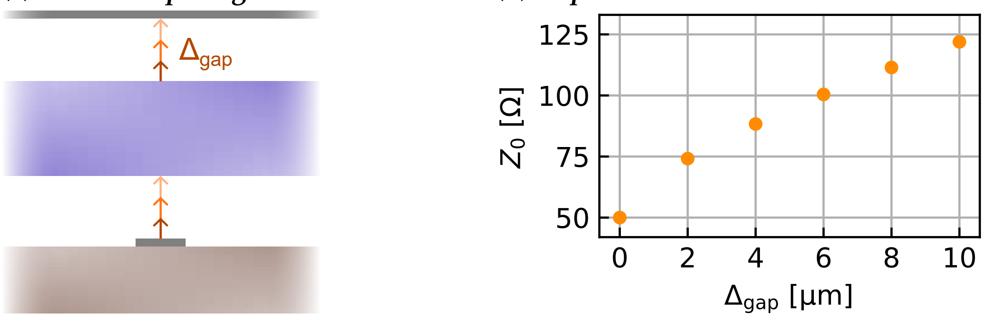

Figure 4.10: Layer gaps: *(a) Undesirable spacing between crystal and top and bottom conductors can be caused by small particles of impurities or broken pieces of membrane. (b) Simulations show a strong dependence of line impedance on distance Δ_{gap} between signal line and membrane as well as membrane and top ground plane of a MS line.*

4.3.5 Electric connections

For measurements of the transmission line chip, it is connected to gold-coated PCBs by aluminum bond wires. Connection quality largely depends on bonding parameters such as power and duration of the ultrasonic pulse melting the wire as well as the force applied to the contacting surface. Interfaces where the wires are attached to the conductor planes of PCB and chip, are the main source of reflections due to impedance mismatches. Oxidized or polluted surfaces shrink the ability to form a proper galvanic connection. SMA connectors are attached to the PCBs to transfer the signal further to coaxial cables used to connect the measurement setup. Here, it is important to ensure the center pin makes contact with the signal line of the PCB to avoid losses to faulty connections. A fully contacted sample is shown in Figure 4.11. Generally, every connection within the

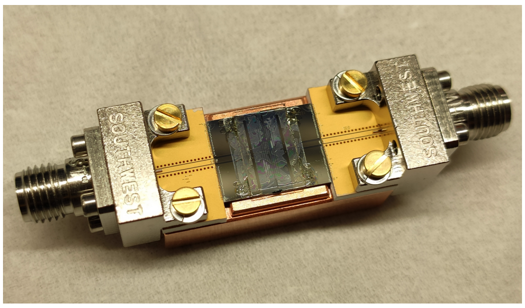

Figure 4.11: Electric contacts: *Tapers of the transmission line chip are connected to a PCB on either side by bond wires. Microwave signals enter and leave the sample through coaxial SMA connectors. (Sample 15M)*

setup potentially gives rise to reflections and losses. Between two points of unmatched impedance, standing waves fulfilling the resonance condition form. This effect will eventually distort a frequency spectrum recorded by regular oscillations in transmission. Resonances may occur between connections to the sample but also between ends of unmatched cables.

Chapter 5

Power-dependent transmission spectra

The transmission of the fabricated chips can be analyzed by applying a continuous microwave signal at one port and comparing it to the transmission received at the second port. Repeating this measurement for a range of frequencies results in a spectrum displaying the frequency response of the sample. Apart from the transmitted amplitude described by the S_{21} scattering parameter, phase and electric delay are recorded. Ideally, the waveguide should support all frequencies equally well, yielding a flat transmission curve apart from signatures caused by the spin system. At frequencies matching a transition of hyperfine levels, photons can be absorbed by the REIs. This leads to a reduced total transmission at the second port and hence appears as a dip in the spectrum. In the real experiment however, detection of the absorptions by spins is obstructed by many factors: Parasitic absorptions, dissipations and reflections caused by mismatches in fabrication as well as by frequency responses of other microwave components like amplifiers and circulators. As the absorption of the highly diluted spin ensemble is small compared to these effects, which can alter the transmission amplitude by several orders of magnitude, a sole spectrum is insufficient to infer the existence of spin absorptions. To this end, the absolute signal power of the frequency sweeps is varied. By comparing their relative transmission, all spectra coincide while power-dependent features manifest in a gradual increase or decrease in transmission magnitude. In the spin system, a high-power excitation depletes the ground state until absorption saturates and relative transmission increases. At the same time, a higher signal power enlarges the interaction volume as the fields penetrate deeper into the crystal. This means a larger number of ions potentially absorbing photons and hence reduced transmission. Another mechanism arises if an allowed transition from an initially empty level exists that is populated upon relaxation of spins from an excited level of another transition. With rising power, a larger number of spins relax to the empty level and can subsequently be addressed by the microwave, again reducing the transmission. These counteracting effects can either lead to an intensifying peak or dip for higher powers. In fact, getting an estimate on the interplay of mechanisms requires probabilities for an absorption by the ions when experiencing a given microwave field within the mode volume of the transmission line and extensive knowledge about allowed transitions in the level structure that are not easily accessible.

5.1 Measurement setup

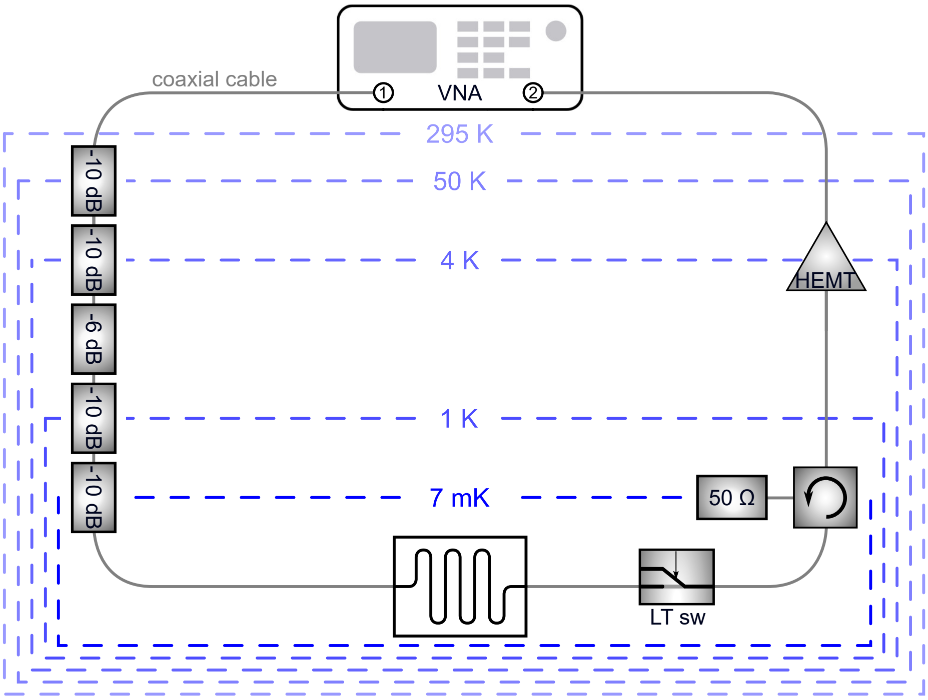

Figure 5.1: Experimental setup for transmission measurements: *The signal coming from port 1 of the VNA is attenuated at different temperature stages of the cryostat by a total of* −46 dB *to block thermal noise photons from the sample input. Multiple samples (only one shown here) can be measured at the mixing chamber stage (*7 mK*) using only one output line of the cryostat by combining their outputs in a low-temperature switch (LT sw). Terminating one port of the circulator by* 50 Ω *effectively forms an isolator ensuring signal flow away from the samples. A HEMT at the* 4 K *stage amplifies the signal by* 37 dB *to room temperature level where it can be detected by the second port on the VNA.*

Transmission measurements are conducted inside a helium dilution cryostat[1], which is capable of reaching temperatures down to 7 mK at its mixing chamber. Transmission properties are investigated using a VNA[2] connected to the respective sample. From port 1 of the VNA, a coaxial SMA cable is connected to an input

[1]LD 400 from Bluefors.
[2]ZNA from Rohde & Schwarz.

line of the cryostat. Several attenuators along the temperature stages dampen the signal to powers compatible with the cryogenic environment, i.e. not raising the temperature. Total attenuation adds up to $-46\,\mathrm{dB}$. The cable then connects to the sample mounted in a copper box or plate, which is thermally anchored to the mixing chamber flange. All samples have a separate input line but are then combined into a single output by a low-temperature switch. This way, each sample can be selected for measurement. Past the switch, superconducting coaxial cables connect to a circulator at the mixing chamber stage, which is terminated by $50\,\Omega$ at one port to force the propagation direction of microwaves away from the switch. All samples are hence isolated from thermal noise photons of higher temperature stages but also from backaction of the amplifier. A high electron mobility transistor (HEMT) at $4\,\mathrm{K}$ amplifies the signal to a level distinguishable from room temperature noise. Finally, the chain is closed by linking to the second port of the VNA. An overview of the experimental setup is given in Figure 5.1.

The final transmission recorded at the VNA is governed by partial losses and reflections of components in the setup. Circulator and HEMT each have their optimal working ranges in which they exhibit high transmission and gain, respectively. The circulator used for measurements in the cryostat exhibits continuously high transmission within $2.2-6\,\mathrm{GHz}$ and the HEMT an average gain of $37\,\mathrm{dB}$ over a frequency span of $0.3-14\,\mathrm{GHz}$.

5.2 Room temperature transmission

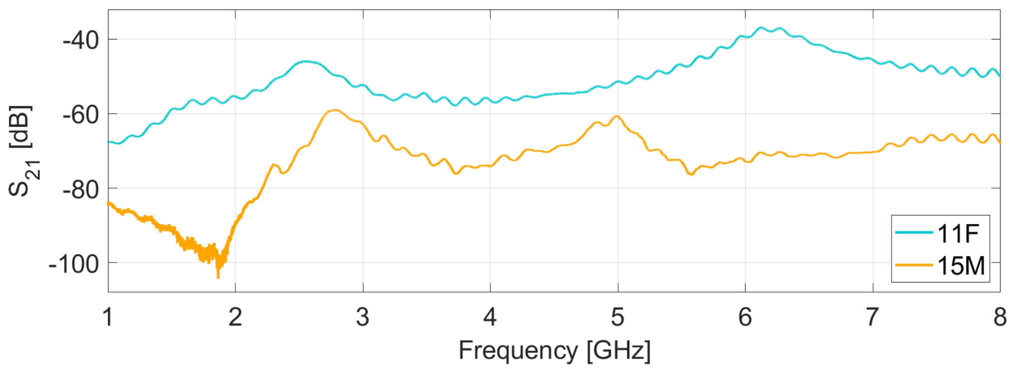

Figure 5.2: Room temperature spectrum: *To check general transmission and electric connections, we record the* S_{21} *parameter at room temperature. The full-ground (11F) and meandering-ground (15M) transmission line chips are directly connected to the VNA at an output power of* $0\,\mathrm{dBm}$.

At room temperature, the setup simplifies by omitting all attenuating and amplifying components needed to measure inside the cryostat. Instead, the transmission line chip can directly be connected to the VNA. Since the spectrum is now unaffected by the setup except for one pair of cables, we get a more precise picture of the transmission line's performance. However, the small line dimensions of the niobium line cause high resistive losses at room temperature. Furthermore, dielectric dissipation limits the transmission. Room temperature spectra of one full-ground and meandering-ground chip are shown in Figure 5.2. The regular oscillations in transmission are believed to result from standing waves in the cables as they were similarly observed for all other samples with a differing length of the meandering signal line. Since the energy levels of the REIs are thermally populated and a low signal-to-noise ratio at ambient conditions dominates the measurement, we do not expect the detection of spin transitions. It rather serves as a control check to ensure electric contact and if there is transmission over the relevant frequency range before cooling down in the cryostat.

5.3 Cryogenic temperature

At millikelvin temperatures, niobium becomes superconducting and the REI spins are in their energetic ground state. To detect them, a power sweep is performed. Starting at the lowest power, the frequency range is swept several times to take averages. This procedure is repeated at an elevated power until the maximum power is reached. The highest power is chosen low enough to not cause noticeable heating of the mixing chamber stage. Additionally, for all samples, an upper power threshold is observed at which the transmission globally decreases. Power-dependent features are overlaid by this background dependence and are difficult to detect without a refined normalization scheme. The highest power is therefore chosen low enough to avoid this effect.

The raw spectrum is obstructed by the operation windows of components in the measurement setup like low-temperature switch, circulator and amplifier. Especially the spectrum of the circulator envelops the sample spectra, as shown in Figure 5.3. Also, resonances, which are assumed to result from impedance mismatches at the connection of coaxial cables, connectors to PCBs or wire bonds, overlay the measurement and cause oscillations in transmission over several dB.

For convenient visualization of power dependent features the spectra are normalized to the highest power by subtraction (Figure 5.4). The full-ground samples (09F, 11F, 14F) receive a generally weaker response of the power-dependent features. Compared to the meandering-ground lines (15M, 16M), they exhibit an decreased signal-to-noise ratio with some feature sizes on the scale of the noise level. The enhanced coupling is expected for the PL design, due to its higher filling factor and increased field homogeneity compared to the MS lines. The large peaks in the normalized data result from large power dependencies of parasitic transmission dips (cf. raw spectra in Figure 5.3) and are accounted as background noise. They are truncated in the plots for better visibility of smaller features. The shape

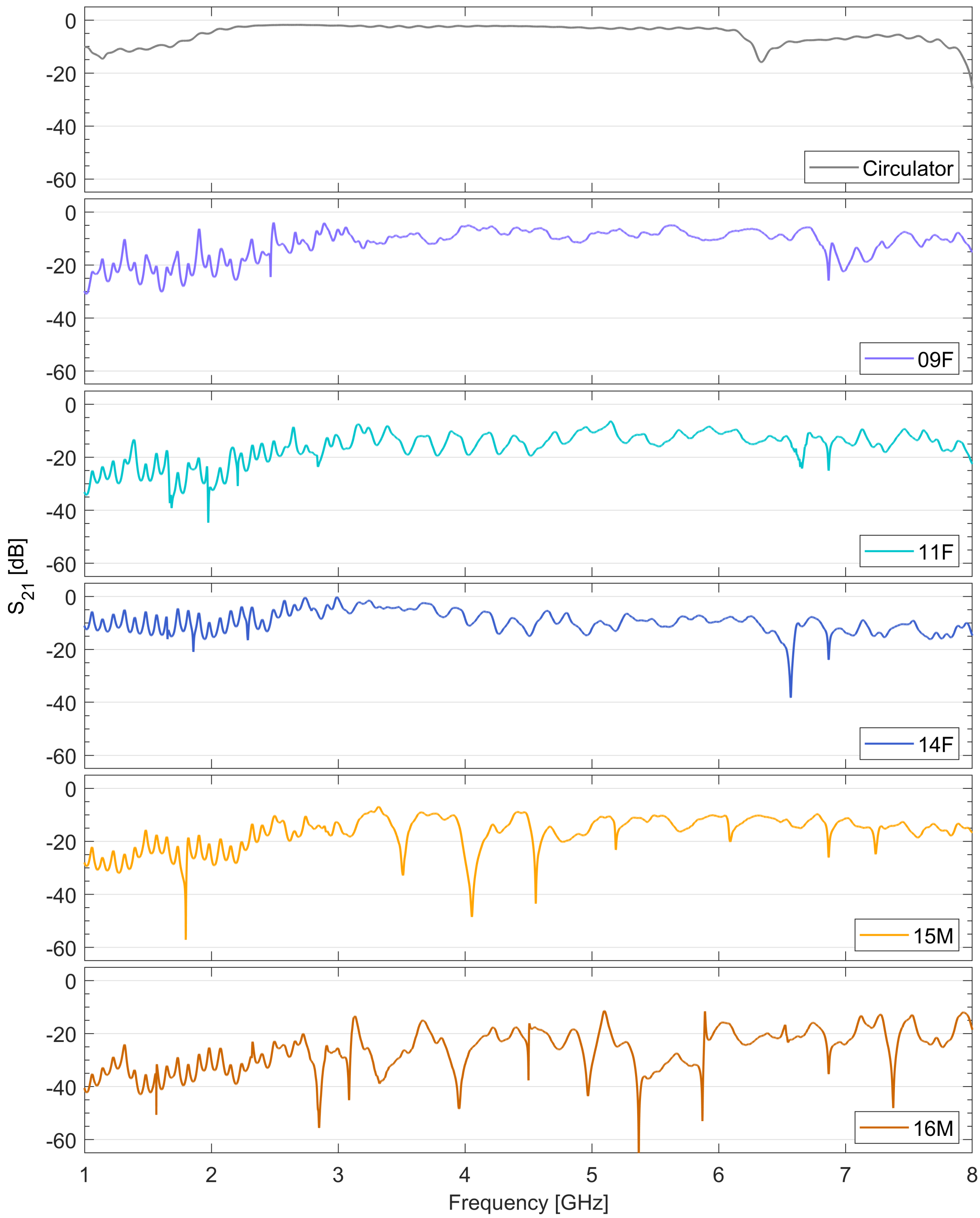

Figure 5.3: Transmission at cryogenic temperatures: *The transmission for all samples was recorded at* 12 mK *with a power of* −16 dBm *at the output of the VNA. The spectra are governed by transmission spectra of all components in the measurement setup, such as the circulator (top).*

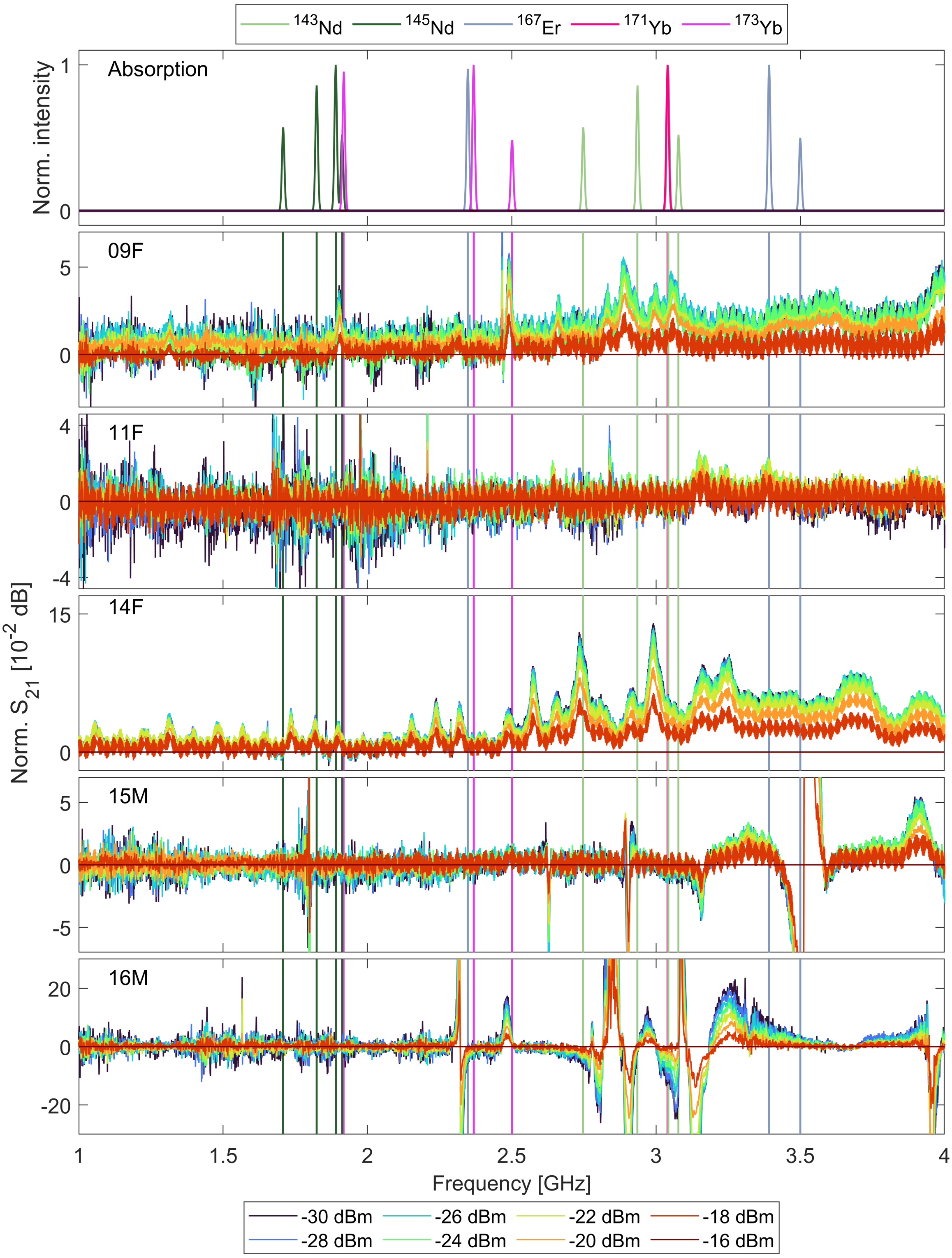

Figure 5.4: Power dependencies: *By normalizing the spectra from Figure 5.3 to the highest power, power-dependent features can be visualized. Normalized absorption of transitions with non-zero intensities of five REIs are shown in the top plot. For details, see main text.*

of an absorption depends on the background transmission as they can couple to resonances in the line.

To compare the features with absorptions of REIs, we overlay simulations of potential candidates for impurities in the ultrapure membrane. Following Abragam and Bleaney, the matrix elements of the principle axes of the **g** and **A** tensors are connected to a pair of constants g_J and A_J by the relation

$$\frac{A_J}{g_J} = \frac{A_a}{g_a} = \frac{A_b}{g_b} = \frac{A_c}{g_c}, \tag{5.1}$$

where g_J is the Landé value for the ground state and A_J is the magnetic hyperfine constant of the free tripositive ion [45]. Given measurements of the g factors in $CaWO_4$ [39, 46, 47], we can estimate the anisotropic hyperfine tensor inside the host crystal without measuring. We could not identify a proper fit of the simulated absorption spectra to frequencies of detected features. A possible explanation is that the quadrupole interaction is not negligible at zero-field. Frequency shifts and additional splitting are therefore not captured in the simulation. Furthermore, as the crystal is highly diluted, the coupling to the ions might not be strong enough to generate a detectable signal. Primarily transitions of reduced probability (intensity in the simulation) within one ion might not be visible. That most frequencies of power-dependent features do not match between samples, might be a result of large fabrication differences that cause varying sensitivity in the detection of spin transitions. There are also multiple unidentified power dependencies in the range from $4-8\,\mathrm{GHz}$. Due to their large frequencies in near-zero magnetic field, we suspect ions with large hyperfine parameters. Potential candidates are ^{165}Ho and ^{141}Pr, however their transitions in this range have zero intensity in the present configuration of crystal to microwave magnetic field.

To summarize, although some frequencies match the simulations, the bare power sweep is not sufficient to draw strong conclusions. The spin transitions can not be distinguished from parasitic resonances in the line with certainty. In fact, their line shape is highly affected by potential coupling to this background. However, utilizing their field dependence allows for identifying actual spin transitions in the spectra. By applying an external magnetic field, the transition frequencies shift according to the Zeeman interaction. This way, absorption as a function of frequency and field can be mapped out. Verifying with simulation, also the spin species could be determined.

Chapter 6

Conclusion

EPR is a powerful method for investigating various classes of materials. For the application in quantum information processing, solid-state systems of REIs have been identified as promising candidates due to their long coherence times of spin transitions [34]. Although cavities are commonly used to couple electromagnetic excitations to the spin system, a non-resonating waveguide offers more flexibility in terms of frequency range. While spin transitions need to be tuned to the resonance frequency of the cavity by an external magnetic field, a transmission line approach allows addressing multiple transitions simultaneously and independent of field in one device. To coherently address a large subensemble of spins, it is necessary to provide a uniform microwave field across a large sample volume.

In this work, we describe the fabrication of planar transmission lines based on a thin crystalline membrane of $CaWO_4$ with a thickness of 20 µm. The hyperfine levels of REIs embedded in the crystal give rise to transitions at GHz frequencies. To detect them, the transmission lines are designed and optimized for high transmission in the range where spin transitions are to be expected. Two different waveguide types, MS and PL, are investigated in terms of impedance and magnetic field distribution. Since in these geometries the signal and ground conductors enclose the crystal, their modes provide the highest field density inside the crystal, while homogeneous in strength and orientation. The chapter on transmission line design describes the structure and layout of the samples and in particular the transition from the CPW to both planar modes. This is accomplished by introducing a top ground plane at CPW dimensions small with respect to membrane thickness and gradually widening the coplanar gaps to infinity forming the MS. The PL emerge from narrowing the top ground plane down to line dimensions. To prevent signal reflections at these transitions, electromagnetic solver software was used for the optimization of line dimensions to maintain an impedance of 50 Ω. For the sample fabrication, we employed optical lithography on niobium thin films sputtered on silicon and sapphire substrates to shape line geometries of the transmission line. Procedures for alignment of membrane and top chip involve markers patterned into the layouts of the chips. The alignment achieved is sufficiently accurate with respect to signal line dimensions. Finally, limitations restricting the quality of the samples are identified and discussed. Primarily, gaps between membrane and conductors drastically increase characteristic impedance and reduce filling factor by altering line geometry. This in turn leads to reflections at unmatched interfaces. For transmission measurements the samples were placed inside a helium dilution cryostat capable of reaching mK temperatures. In the cryogenic environment, the niobium conductors become superconducting reducing the dissipation of the system. Although the spectra are affected by resonance effects and operating windows of components in the measurement setup, multiple power-dependent features were identified. Especially the full-ground samples suffer from a low signal-to-noise ratio. A strong power dependence of the background limits the accessible range to low powers where features are not easily detected. More refined normalization schemes would be required to extract information. We provide a comparison of the power-dependent signatures to simulated absorption spectra of REIs. However, limited access to experimentally verified hyperfine and quadrupole tensors in $CaWO_4$ restricts the accuracy of simulations in near-zero fields.

To use the planar transmission lines to their full capacity, fabrication techniques need to be improved in terms of sample cleanliness. As most impurities causing layer gaps stem from particle inclusions in the glue of the polished membrane, a significant enhancement is to be expected by optimizing this fabrication step. A possibility would be to glue the slab of crystal in a cleanroom environment with pure glue before polishing to avoid contamination when ungluing the membrane from its glass holder. Another way would be to polish down the crystal while already placed on the bottom chip. Reducing its plane dimensions might help with reducing the membrane's sensitivity to breaking into pieces and, therefore, reducing the number of shards that can get trapped between layers.

To investigate the recorded transmission spectra in more detail the samples can be placed inside an external magnetic field. Due to the field dependence of the electronic Zeeman interaction, energetic levels and hence transition frequencies of the REIs shift. Repeating the power-sweep measurement at various magnetic field strengths yields a map revealing their field- and frequency-dependent energy landscape. Due to the broadband applicability of the cavity-free approach, this works also in the range where field-independent interactions are not yet negligible. In particular, the zero-field splitting can be accessed directly. This allows for a detailed analysis and measurement of parameters in the spin Hamiltonian.

Appendix A

Transmission line parameters

The line parameters of the samples simulated (Chapter 3), fabricated (Chapter 4) and measured (Chapter 5) within this work are listed in Table A.1. They are visualized in Figure A.1 for the full-ground design and Figures A.2 and A.3 for the meandering-ground design. In particular, the optimized parameters for MS and ground transitions are given in Table A.3. Table A.2 lists dimensions of the dielectric substrates and the crystalline membrane.

Table A.1: Line parameters: *The number in brackets after the sample name denotes the number of meander turns. All dimensions are given in* µm. *The total lengths of the planar transmission line sections (between two MS/ground transitions) are given in the last row.*

Sample name	09F (**6**)	11F (**4**)	14F (**8**)	15M (**4**)	16M (**6**)
taper patch length	1768	2000	2000	2000	2000
taper patch width	500	500	500	500	500
taper patch gap	232	232	232	232	232
taper length	1000	1000	1000	1000	1000
sandwiched line length	0	0	0	1000	1000
sandwiched line width	5.00	5.00	5.00	5.00	5.00
sandwiched gap	8.13	8.13	8.13	8.27	8.27
MS transition length	1000	1000	1000	300	300
transition line width	-	-	-	10.61	10.61
ground transition length	-	-	-	500	300
ground line width	-	-	-	32.60	32.60
top ground width	-	-	-	8000	8000
planar line width	10.61	10.61	10.61	16.00	16.00
meander gap	280	200	180	200	190
meander width	7000	6000	6000	6000	6000
Total line length	86251	51102	98439	49438	73459

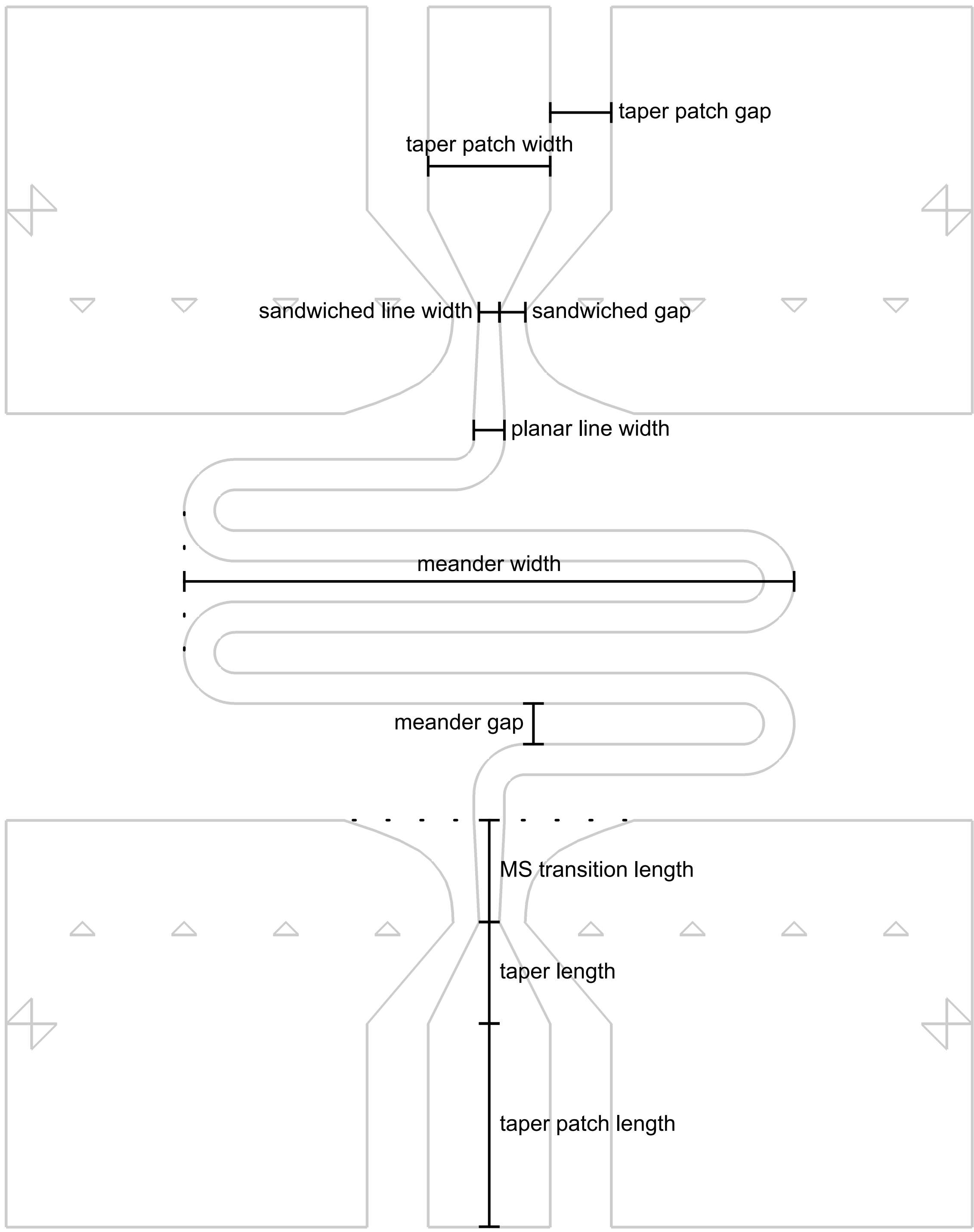

Figure A.1: Schematic visualization of line parameters for the bottom chip in full-ground design.

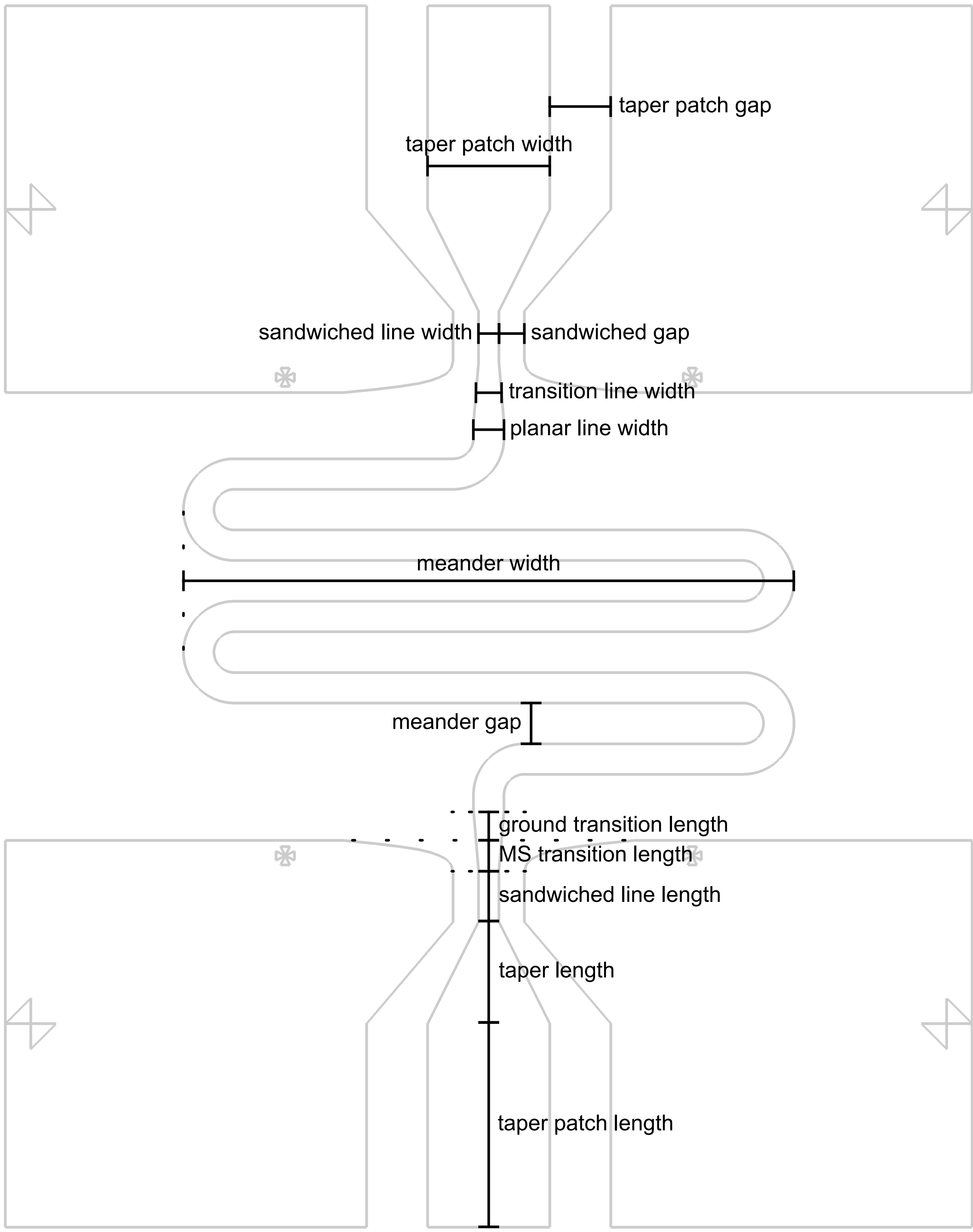

Figure A.2: Schematic visualization of line parameters for the bottom chip in meandering-ground design.

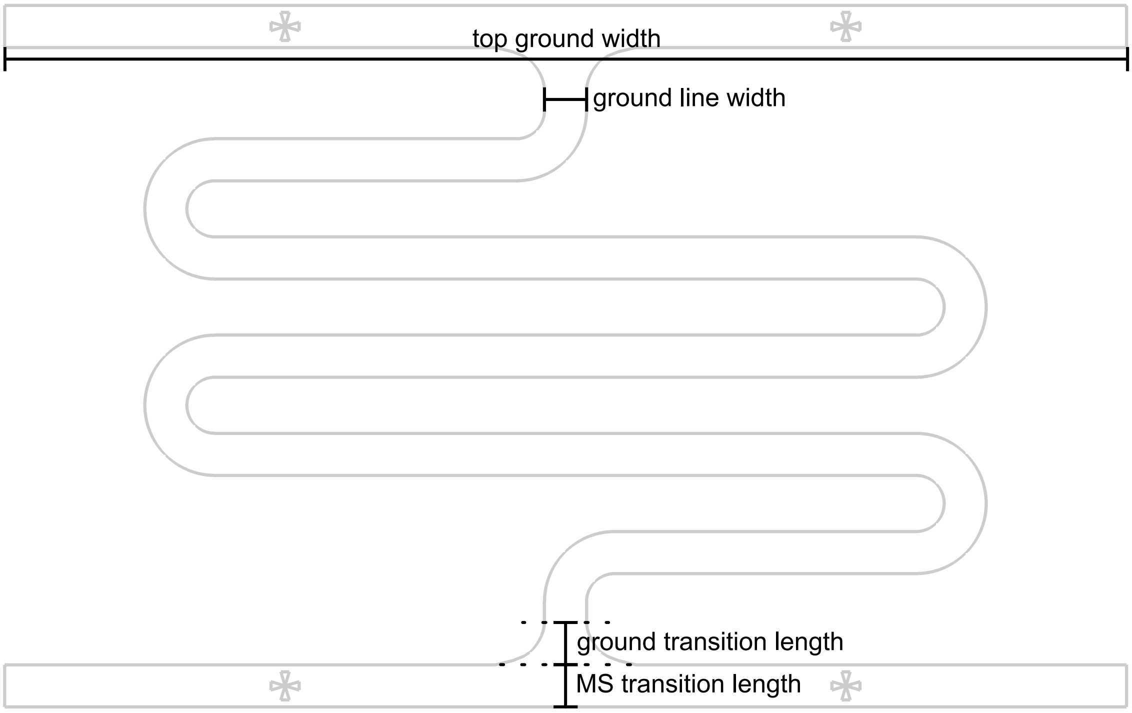

Figure A.3: Schematic visualization of line parameters for the top chip in meandering-ground design.

Table A.2: Substrate dimensions.

	Length [mm]	Width [mm]	Thickness [µm]
Membrane ($CaWO_4$)	8	9	20
Bottom chip (Si)	12	9.5	525
Top chip (Si)	6	10	525
Top chip (Al_2O_3)	6	10	430

Table A.3: Optimized transition parameters: *The coplanar gap (left) and the width of the ground line (right) are optimized to maintain the characteristic impedance of* 50 Ω *for the widening signal line along the MS and ground transition, respectively. For values marked with* **, the optimization did not converge. All dimensions are given in* μm*.*

signal line width	coplanar gap
5.00	9.598
5.25	10.224
5.50	10.899
5.75	11.611
6.00	12.395
6.25	13.266
6.50	14.129
6.75	15.123
7.00	16.226
7.25	17.433
7.50	18.839
7.75	20.419
8.00	22.263
8.25	24.515
8.50	27.285
8.75	30.993
9.00	36.811
9.25	47.900
9.50	62.756
9.75	88.000
10.00	130.783
10.25	230*
10.50	600*

signal line width	ground line width
11.0	76.525
11.5	64.287
12.0	56.528
12.5	50.951
13.0	46.961
13.5	43.286
14.0	40.498
14.5	38.203
15.0	36.126
15.5	34.143

Appendix B

Fabrication recipes and techniques

This chapter provides more detailed information about the fabrication and assembly of the transmission line chips in addition to the main description in Chapter 4. The fabrication of niobium thin films for this work relies on existing procedures described by Bruckmoser [44]. All recipes for the machines were created and optimized by experienced members of the fabrication-team at the Walther-Meissner-Institute.

B.1 Thin films

Substrate cleaning

- Preheat a beaker filled with acetone p.a. on a hot plate set to 80 °C for ≈ 2 min
- Insert the substrate into the beaker and keep heating for 2 min
- Put the beaker in an ultrasonic bath set to power 9/9 (5/9 for metallized substrates) for 2 min
- Repeat above steps with a beaker filled with isopropanol p.a.
- Blow dry substrate with N_2

Sputtering

Target power [W]	Duration [s]	Pressure [mTorr]
300	450	4

Spincoating + prebake

AZ MIR 701[1] (positive)/ma-N 1420[2] (negative) resist for the bottom chips (14.3×14.3 mm^2)/meandering-ground top chip (6×10 mm^2).

- Apply 70 µL/50 µL of the respective resist at the center of the substrate
- Spin for 60 s/60 s with 4000 rpm @ 1500 $\frac{rpm}{s}$ / 8000 rpm @ 2000 $\frac{rpm}{s}$
- Bake on hot plate at 90 °C/90 °C for 75 s/120 s

Optical lithography

	Exposure energy [mJ/cm^2]	Spot size [nm]	Scan speed [mm/s]
AZ MIR 701	120	300	30
ma-N 1420	250	300	50

Postbake + developing

AZ MIR 701/ma-N 1420

- Bake chip on hot plate at 110 °C/100 °C for 90 s/60 s
- Swing the chip in AZ 726 MIF/ma-D 533/S in a ∞-pattern for 70 s/360 s
- Rinse with H_2O p.a. and proceed swinging in a beaker filled with H_2O p.a. for at least 10 s
- Repeat previous step with fresh H_2O p.a.
- Blow dry substrate with N_2

Reactive-ion etching

Etch time [s]	SF_6 flow [sccm]	RF power [W]	Pressure [mTorr]
170	10	100	12

[1] From MicroChemicals.
[2] From micro resist technology.

Stripping

- Place the chip in a beaker filled with TechniStrip P1331[3] and run the ultrasonic bath on power 5/9 for 2 min
- Place the beaker on a hot plate set to 80 °C for 5 min
- Rinse with H_2O p.a. and swing in a beaker filled with H_2O p.a. in a ∞-pattern for at least 10 s
- Repeat previous step with fresh H_2O p.a.
- Blow dry substrate with N_2

B.2 Membrane placement

For placement of the membrane on the superconducting chip, the thermoplastic glue is dissolved in acetone p.a. However, the number of handling steps should be low to avoid breaking the membrane. To this end, the patterned bottom chip is placed inside a beaker filled with acetone. The glass plate is put on top with the membrane facing down. Copper tape is applied to the glass plate around the membrane to serve as a spacer. This way only the copper is in contact with the chip while the membrane keeps a small distance. When the glue is dissolved, the membrane will detach from the glass plate and drop directly onto the chip. The plate including copper tape can be removed from the beaker without touching the membrane. Next, the acetone is removed with a pipette until the level drops below the surface of the chip. Otherwise, there is a risk of washing the membrane off the chip. Now the chip is put into a fresh beaker that is then slowly filled with isopropanol p.a. By carefully swinging the beaker, chip and membrane are cleaned from acetone residuals. After again removing the chemical from the beaker first, the chip is dried with low-pressure nitrogen. The membrane will stick to the chip enough by adhesion to not be blown off.

B.3 Top chip alignment

To assert the top chip is parallel to the bottom chip, the top chip is picked up with the mounted tweezers while lying on a clean surface (e.g. a microscope slide) with the metallized surface facing down. It is then lifted above the bottom chip using the vertical translation stage. The bottom chip with glued crystal is placed on a microscope slide and focused with the microscope at a magnification where at least two markers around one of the MS transitions are visible. The top chip is

[3]From MicroChemicals.

moved into the field of view and lowered until the edge of the full-ground chip or cross markers are close to the focal point without touching the crystal yet. It is to note that the ocular might need to be adjusted to focus the markers again as the sapphire slightly shifts the focal point. The microscope slide including the bottom chip is carefully rotated until both chips are parallel. Horizontal alignment is completed using the translation table of the microscope. When aligned, the top chip is lowered further until contact with the membrane.

Bibliography

[1] J. I. Cirac and P. Zoller. A scalable quantum computer with ions in an array of microtraps. *Nature*, 404(6778):579, 2000.

[2] I. Pogorelov, T. Feldker, Ch. D. Marciniak, L. Postler, G. Jacob, O. Krieglsteiner, V. Podlesnic, M. Meth, V. Negnevitsky, M. Stadler, B. Höfer, C. Wächter, K. Lakhmanskiy, R. Blatt, P. Schindler, and T. Monz. Compact ion-trap quantum computing demonstrator. *PRX Quantum*, 2:020343, 2021.

[3] C. Gross and I. Bloch. Quantum simulations with ultracold atoms in optical lattices. *Science*, 357(6355):995, 2017.

[4] S. Ebadi, T. T. Wang, H. Levine, A. Keesling, G. Semeghini, A. Omran, D. Bluvstein, R. Samajdar, H. Pichler, W. W. Ho, S. Choi, S. Sachdev, M. Greiner, V. Vuletić, and M Lukin. Quantum phases of matter on a 256-atom programmable quantum simulator. *Nature*, 595(7866):227, 2021.

[5] J. R. Weber, W. F. Koehl, J. B. Varley, A. Janotti, B. B. Buckley, C. G. Van de Walle, and D. D. Awschalom. Quantum computing with defects. *Proceedings of the National Academy of Sciences*, 107(19):8513, 2010.

[6] L. Childress and R. Hanson. Diamond NV centers for quantum computing and quantum networks. *MRS Bulletin*, 38(2):134, 2013.

[7] F. Arute, K. Arya, R. Babbush, D. Bacon, J. C. Bardin, R. Barends, R. Biswas, S. Boixo, F. G. S. L. Brandao, D. A. Buell, B. Burkett, Y. Chen, Z. Chen, B. Chiaro, R. Collins, W. Courtney, A. Dunsworth, E. Farhi, B. Foxen, A. Fowler, C. Gidney, M. Giustina, R. Graff, K. Guerin, S. Habegger, M. P. Harrigan, M. J. Hartmann, A. Ho, M. Hoffmann, T. Huang, T. S. Humble, S. V. Isakov, E. Jeffrey, Z. Jiang, D. Kafri, K. Kechedzhi, J. Kelly, P. V. Klimov, S. Knysh, A. Korotkov, F. Kostritsa, D. Landhuis, M. Lindmark, E. Lucero, D. Lyakh, S. Mandrà, J. R. McClean, M. McEwen, A. Megrant, X. Mi, K. Michielsen, M. Mohseni, J. Mutus, O. Naaman, M. Neeley, C. Neill,

M. Y. Niu, E. Ostby, A. Petukhov, J. C. Platt, C. Quintana, E. G. Rieffel, P. Roushan, N. C. Rubin, D. Sank, K. J. Satzinger, V. Smelyanskiy, K. J. Sung, M. D. Trevithick, A. Vainsencher, B. Villalonga, T. White, Z. J. Yao, P. Yeh, A. Zalcman, H. Neven, and J. M. Martinis. Quantum supremacy using a programmable superconducting processor. *Nature*, 574(7779):505, 2019.

[8] G. Kurizki, P. Bertet, Y. Kubo, K. Mølmer, D. Petrosyan, P. Rabl, and J. Schmiedmayer. Quantum technologies with hybrid systems. *Proceedings of the National Academy of Sciences*, 112(13):3866, 2015.

[9] A. A. Clerk, K. W. Lehnert, P. Bertet, J. R. Petta, and Y. Nakamura. Hybrid quantum systems with circuit quantum electrodynamics. *Nature Physics*, 16 (3):257, 2020.

[10] C. Grèzes, Y. Kubo, B. Julsgaard, T. Umeda, J. Isoya, H. Sumiya, H. Abe, S. Onoda, T. Ohshima, K. Nakamura, I. Diniz, A. Auffèves, V. Jacques, J. Roch, D. Vion, D. Esteve, K. Mølmer, and P. Bertet. Towards a spin-ensemble quantum memory for superconducting qubits. *Comptes Rendus Physique*, 17(7):693, 2016.

[11] É. Gouzien and N. Sangouard. Factoring 2048-bit RSA integers in 177 days with 13 436 qubits and a multimode memory. *Physical Review Letters*, 127(14): 140503, 2021.

[12] M. Afzelius, C. Simon, H. De Riedmatten, and N. Gisin. Multimode quantum memory based on atomic frequency combs. *Physical Review A*, 79(5):052329, 2009.

[13] W. J. Munro, K. Azuma, K. Tamaki, and K. Nemoto. Inside quantum repeaters. *IEEE Journal of Selected Topics in Quantum Electronics*, 21(3):78, 2015.

[14] N. Lauk, N. Sinclair, S. Barzanjeh, J. P. Covey, M. Saffman, M. Spiropulu, and C. Simon. Perspectives on quantum transduction. *Quantum Science and Technology*, 5(2):020501, 2020.

[15] C. Simon, M. Afzelius, J. Appel, A. Boyer de la Giroday, S. J. Dewhurst, N. Gisin, C. Y. Hu, F. Jelezko, S. Kröll, J. H. Müller, J. Nunn, E. S. Polzik, J. G. Rarity, H. De Riedmatten, W. Rosenfeld, A. J. Shields, N. Sköld, R. M. Stevenson, R. Thew, I. A. Walmsley, M. C. Weber, H. Weinfurter, J. Wrachtrup, and R. J. Young. Quantum memories: A review based on the european integrated project "qubit applications (QAP)". *The European Physical Journal D*, 58: 1, 2010.

[16] C. W. Thiel, T. Böttger, and R. L. Cone. Rare-earth-doped materials for applications in quantum information storage and signal processing. *Journal of Luminescence*, 131(3):353, 2011.

[17] V. Ranjan, J. O'Sullivan, E. Albertinale, B. Albanese, T. Chanelière, T. Schenkel, D. Vion, D. Esteve, E. Flurin, J. J. L. Morton, and P. Bertet. Multimode storage of quantum microwave fields in electron spins over 100 ms. *Physical Review Letters*, 125(21):210505, 2020.

[18] C. Grèzes, B. Julsgaard, Y. Kubo, M. Stern, T. Umeda, J. Isoya, H. Sumiya, H. Abe, S. Onoda, T. Ohshima, V. Jacques, J. Esteve, D. Vion, D. Esteve, K. Mølmer, and P. Bertet. Multimode storage and retrieval of microwave fields in a spin ensemble. *Physical Review X*, 4(2):021049, 2014.

[19] J. O'Sullivan, O. W. Kennedy, C. W. Zollitsch, M. Šimėnas, C. N. Thomas, L. V. Abdurakhimov, S. Withington, and J. J. L. Morton. Spin-resonance linewidths of bismuth donors in silicon coupled to planar microresonators. *Physical Review Applied*, 14(6):064050, 2020.

[20] H. Hübl, C. W. Zollitsch, J. Lotze, F. Hocke, M. Greifenstein, A. Marx, R. Gross, and S. T. B. Goennenwein. High cooperativity in coupled microwave resonator ferrimagnetic insulator hybrids. *Physical Review Letters*, 111(12):127003, 2013.

[21] J. S. Hyde, R. R. Mett, and J. R. Anderson. Cavities with axially uniform fields for use in electron paramagnetic resonance. III. Re-entrant geometries. *Review of Scientific Instruments*, 73(11):4003, 2002.

[22] S. K. Misra. *Multifrequency Electron Paramagnetic Resonance: Theory and Applications*. John Wiley & Sons, 2011.

[23] R. N. Simons. *Coplanar Waveguide Circuits, Components, and Systems*. John Wiley & Sons, 2004.

[24] S. S. Bedair and I. Wolff. Fast, accurate and simple approximate analytic formulas for calculating the parameters of supported coplanar waveguides for (M) MIC's. *IEEE Transactions on Microwave Theory and Techniques*, 40(1):41, 1992.

[25] I. J. Bahl and R. Garg. Simple and accurate formulas for a microstrip with finite strip thickness. *Proceedings of the IEEE*, 65(11):1611, 1977.

[26] R. Schinzinger and P. A. A. Laura. *Conformal Mapping: Methods and Applications*. Courier Corporation, 2012.

[27] C. Clauß. *On-Chip Broadband Magnetic Resonance Spectroscopy Down to Ultralow Temperatures*. PhD thesis, University of Stuttgart, 2014.

[28] S. Gevorgian, L. J. P. Linner, and E. L. Kollberg. CAD models for shielded multilayered CPW. *IEEE Transactions on Microwave Theory and Techniques*, 43 (4):772, 1995.

[29] C. P. Poole. *Electron Spin Resonance: A Comprehensive Treatise on Experimental Techniques*. Courier Corporation, 1996.

[30] D. M. Pozar. *Microwave Engineering*. John Wiley & Sons, 2011.

[31] D. Lago-Rivera, S. Grandi, J. V. Rakonjac, A. Seri, and H. De Riedmatten. Telecom-heralded entanglement between multimode solid-state quantum memories. *Nature*, 594(7861):37, 2021.

[32] L. A. Williamson, Y. Chen, and J. J. Longdell. Magneto-optic modulator with unit quantum efficiency. *Physical Review Letters*, 113(20):203601, 2014.

[33] X. Fernandez-Gonzalvo, Y. Chen, C. Yin, S. Rogge, and J. J. Longdell. Coherent frequency up-conversion of microwaves to the optical telecommunications band in an Er:YSO crystal. *Physical Review A*, 92(6):062313, 2015.

[34] M. Le Dantec, M. Rančić, S. Lin, E. Billaud, V. Ranjan, D. Flanigan, S. Bertaina, T. Chanelière, P. Goldner, A. Erb, R. B. Liu, D. Esteve, D. Vion, E. Flurin, and P. Bertet. Twenty-three–millisecond electron spin coherence of erbium ions in a natural-abundance crystal. *Science Advances*, 7(51):eabj9786, 2021.

[35] K. Momma and F. Izumi. VESTA 3 for three-dimensional visualization of crystal, volumetric and morphology data. *Journal of Applied Crystallography*, 44(6):1272, 2011.

[36] R. M. Hazen, L. W. Finger, and J. W. E. Mariathasan. High-pressure crystal chemistry of scheelite-type tungstates and molybdates. *Journal of Physics and Chemistry of Solids*, 46(2):253, 1985.

[37] J. S. Thorp and E. A. E. Ammar. The dielectric constants of $CaWO_4$, Nd/$CaWO_4$ and Gd/$CaWO_4$. *Journal of Materials Science*, 10:918, 1975.

[38] A. Erb and J. Lanfranchi. Growth of high-purity scintillating $CaWO_4$ single crystals for the low-temperature direct dark matter search experiments CRESST-II and EURECA. *CrystEngComm*, 15(12):2301, 2013.

[39] B. G. Enrique. Optical spectrum and magnetic properties of Er^{3+} in $CaWO_4$. *The Journal of Chemical Physics*, 55(5):2538, 1971.

[40] S. Stoll and A. Schweiger. Easyspin, a comprehensive software package for spectral simulation and analysis in EPR. *Journal of Magnetic Resonance*, 178(1): 42, 2006.

[41] A. Schweiger and G. Jeschke. *Principles of Pulse Electron Paramagnetic Resonance*. Oxford University Press on Demand, 2001.

[42] J. Krupka, J. Breeze, A. Centeno, N. Alford, T. Claussen, and L. Jensen. Measurements of permittivity, dielectric loss tangent, and resistivity of float-zone silicon at microwave frequencies. *IEEE Transactions on Microwave Theory and Techniques*, 54(11):3995, 2006.

[43] R. Gross, A. Marx, D. Einzel, and S. Geprägs. *Festkörperphysik*. De Gruyter, 2018.

[44] N. Bruckmoser. *Development of a Fabrication Process for High-Coherence Niobium Qubits*. Master's thesis, Technical University of Munich, 2021.

[45] A. Abragam and B. Bleaney. *Electron Paramagnetic Resonance of Transition Ions*. Oxford University Press, 2012.

[46] D. Sengupta and J. O. Artman. Energy-level scheme for Nd^{3+} in $CaWO_4$. *The Journal of Chemical Physics*, 50(12):5308, 1969.

[47] J. P. Sattler and J. Nemarich. Electron paramagnetic resonance of Yb^{3+} in scheelite single crystals. *Physical Review B*, 1(11):4249, 1970.

Acknowledgments

At this point, I want to emphasize and appreciate all the amazing people who contributed to and supported me with this work. I thank:

Prof. Dr. Rudolf Gross for providing the opportunity to write my thesis at the Walther-Meißner-Institute. I really enjoyed the time here.

Dr. Nadezhda Kukharchyk for being such a kind advisor, for taking your time for my questions, for always having some constructive and helpful feedback and for never leaving without a smile.

Ana Strinic for your continuous efforts during the measurement time, IT support and for being the first person for me to speak to in most regards.

Niklas Bruckmoser for teaching me virtually everything I know about thin film fabrication and the cleanroom. I admire how you seem to have an answer to every question (and for your bonding skills).

The rest of the mw-RESystems group Owen, Chiun, Lukas and Jianpeng for interesting discussions during lunch and the good teamwork.

My fellow bachelor and master students Max, Tammo, David, Franziska, Julian, Catharina, Raphael, Florian K., Ruben, Aaron, Julius, Jan and Florian M. who shared office 128 with me.

The workshop team for fabricating our sample boxes.

The staff that keeps the WMI running, especially Sybilla and Maria.

The entire WMI for the pleasant working atmosphere.

Prof. Dr. Andreas Erb and Michael Stanger for the preparation of the membranes for this project.

My band members Tobias, Max and Manuel for the good friendship and for keeping me busy on a musical level.

Most of all my family for being so supportive throughout this last year and giving me the freedom to concentrate on my studies. I owe you everything.